The Astrophysical Journal, 758:94 (20pp), 2012 October 20 doi:10.1088/0004-637X/758/2/94

AGN ACTIVITY AND THE MISALIGNED HOT ISM IN THE COMPACT RADIO ELLIPTICAL NGC 4278

Silvia Pellegrini[1], Junfeng Wang[2], Giuseppina Fabbiano[2], Dong-Woo Kim[2],
Nicola J. Brassington[3], John S. Gallagher[4], Ginevra Trinchieri[5], and Andreas Zezas[6]
[1] Department of Astronomy, University of Bologna, via Ranzani 1, I-40127 Bologna, Italy
[2] Harvard-Smithsonian Center for Astrophysics, 60 Garden St, Cambridge, MA 02138, USA
[3] School of Physics, Astronomy, and Mathematics, University of Hertfordshire, Hatfield, UK
[4] Department of Astronomy, University of Wisconsin-Madison, Madison, WI 53706, USA
[5] INAF-Osservatorio Astronomico di Brera, Via Brera 28, I-20121 Milano, Italy
[6] Physics Department, University of Crete, Heraklion, Greece
Received 2012 June 11; accepted 2012 August 20; published 2012 October 4

ABSTRACT

The analysis of a deep (579 ks) *Chandra* ACIS pointing of the elliptical galaxy NGC 4278, which hosts a low-luminosity active galactic nucleus (AGN) and compact radio emission, allowed us to detect extended emission from hot gas out to a radius of ∼5 kpc, with 0.5–8 keV luminosity of 2.4×10^{39} erg s^{-1}. The emission is elongated in the NE–SW direction, misaligned with respect to the stellar body, and aligned with the ionized gas and with the *Spitzer* IRAC 8 μm non-stellar emission. The nuclear X-ray luminosity decreased by a factor of ∼18 since the first *Chandra* observation in 2005, a dimming that enabled the detection of hot gas even at the position of the nucleus. The gas shows a significantly larger temperature ($kT = 0.75$ keV) in both the projected and deprojected profiles in the inner ∼300 pc than in the surrounding region, where it stays at ∼0.3 keV, a value lower than expected from standard gas heating assumptions. The nuclear X-ray emission is consistent with that of a low radiative efficiency accretion flow, accreting mass at a rate close to the Bondi rate; estimates of the power of the nuclear jets require that the accretion rate is not largely reduced with respect to the Bondi rate. Among possible origins for the central large hot gas temperature, such as gravitational heating from the central massive black hole and a recent AGN outburst, interaction with the nuclear jets seems more likely, especially if the latter remain confined, and heat the nuclear region frequently. The unusual hot gas distribution on the galactic scale could be due to the accreting cold gas triggering the cooling of the hot phase, a process also contributing to the observed line emission from ionized gas, and to the hot gas temperature being lower than expected; alternatively, the latter could be due to the efficiency of the Type Ia supernova heating that is lower than usually adopted.

Key words: galaxies: active – galaxies: elliptical and lenticular, CD – galaxies: individual: NGC 4278 – galaxies: nuclei – X-rays: galaxies – X-rays: ISM

Online-only material: color figures

1. INTRODUCTION

In recent years, high angular resolution X-ray observations of early-type galaxies performed with *Chandra* allowed us to investigate extensively the connection between the central supermassive black hole (MBH) and the surrounding hot interstellar medium (ISM; e.g., Forman et al. 2007; Allen et al. 2006; Diehl & Statler 2008; David et al. 2009; Million et al. 2010), a study with important implications for the building of a complete picture of the host-galaxy–MBH coevolution (Silk & Rees 1998; Di Matteo et al. 2005; Hopkins et al. 2005; Merloni & Heinz 2008; Cattaneo et al. 2009; Schawinski et al. 2009; Ciotti et al. 2010; Kaviraj et al. 2011). The investigations so far have concentrated mostly on X-ray bright and massive ellipticals, where the high hot gas surface brightness most clearly reveals signs of feedback heating as cavities, shells, filaments, and edges. For a complete understanding of the MBH–host-galaxy coevolution process, it is, however, important to realize how the activity cycle works even in low- to intermediate-mass galaxies, which are far more numerous, and currently almost unexplored (see Fabbiano et al. 2004; Pellegrini et al. 2007a, 2007b for one of the few exceptional cases, NGC 821). Other aspects that are still unclear include the relationship between the nuclear emission and other galactic properties, such as the fuel availability for the MBH (e.g., Ho 2008; Pellegrini 2010; Gallo et al. 2010), the accretion modalities (standard disk plus hot corona, Haardt & Maraschi 1993, or radiatively inefficient accretion (RIAF; Narayan & Yi 1995; e.g., Ptak et al. 2004; Maoz 2007; Ho 2008), and what determines the partition in the accretion output between radiative and mechanical energies (e.g., Allen et al. 2006; Merloni & Heinz 2007).

In this paper, we analyze two new *Chandra* pointings of the medium-mass elliptical galaxy NGC 4278 ($d = 16.1$ Mpc[7] and $L_B = 1.7 \times 10^{10}\ L_{B,\odot}$; Table 1), obtained in 2010 March; we also consider the data of six previous pointings between 2005 and 2007, totaling 579 ks of net exposure time. With this deep observation, we explore the origin of the nuclear emission and the possible interaction of the active galactic nucleus (AGN) activity with the surrounding hot ISM. The spatially resolved properties of the low surface brightness hot gas could be determined at a high level of accuracy thanks to the long exposure time, the careful subtraction of the emission from stellar sources allowed by the *Chandra* high angular resolution, and the significant dimming of the nucleus during 2010; all this has allowed us to determine the hot gas properties of the central region (down to within a radius of 2″ from the nucleus) and of the more extended galactic body, out to a radius of ∼70″ (∼5 kpc).

[7] At this distance 1″ = 78 pc.

Table 1
General Properties of NGC 4278

D (Mpc) (1)	Morph. Type (2)	B_0^T (Bmag) (3)	$L_B/10^{10}$ ($L_{B,\odot}$) (4)	Optical Class (5)	M_{BH} ($10^8 M_\odot$) (6)	$\sigma_{e/8}$ (km s^{-1}) (7)	R_e ($''$) (8)
16.1	E1+	10.97	1.7	L1.9	3.4	252	32

Notes. Column 1: distance from Tonry et al. (2001); Columns 2 and 3: morphological type and B_0^T from RC3; Column 4: L_B from B_0^T and the adopted distance; Column 5: type of optical nuclear emission (Ho et al. 1997); Column 6: M_{BH} from the $M_{BH} - \sigma$ relation (Tremaine et al. 2002); Column 7: stellar velocity dispersion within a central aperture of $R_e/8$ (Kuntschner et al. 2010); Column 8 effective radius (Cappellari et al. 2006).

NGC 4278 is a relatively isolated elliptical galaxy, belonging to the LGG 279 group of 17 galaxies (Garcia 1993); its morphological type is E1-2, it has a regular optical shape, and a uniformly old stellar population (Shapiro et al. 2010; Kuntschner et al. 2010). NGC 4278 also hosts a LINER1 nucleus, with a weak broad component in the optical Hα line (Ho et al. 1997). Unlike standard AGNs, NGC 4278 shows a low level X-ray nuclear emission ($\sim 10^{40}$ erg s^{-1}; Younes et al. 2010), and a very sub-Eddington bolometric emission (5×10^{-6}; Eracleous et al. 2010a; Nemmen et al. 2011). This LINER is known to be radio loud (Terashima & Wilson 2003) and has been deeply studied in the radio. At arcsecond resolution, the Very Large Array (VLA) shows an unresolved emission from 5 to 43 GHz (Wrobel & Heeschen 1984; Nagar et al. 2001), while an extended structure is visible at milliarcsecond resolution with very long baseline interferometry (VLBI) at 18 and 6 cm (Schilizzi et al. 1983), and a parsec-scale two-sided radio jet was resolved by the Very Long Baseline Array (VLBA) emerging from a central compact component (Giroletti et al. 2005). The highly bent jet morphology suggests that the jet may be interacting with the ambient medium in the inner few parsecs. The total radio (VLA) luminosity is $P_{1.4\ \mathrm{GHz}} = 1.0 \times 10^{21.7}$ W Hz^{-1} (Giroletti et al. 2005 for our adopted distance), and then at least two orders of magnitude lower than in powerful radio-loud AGNs.

NGC 4278 finally hosts a multiphase ISM. The SAURON survey (Sarzi et al. 2006) revealed strong emission from ionized gas in the central region, whose kinematical structure is consistent with that inferred for a massive ($M_{\mathrm{H\,I}} = 6.9 \times 10^8\ M_\odot$), extended (with a diameter of 37 kpc), and regular H I disk (Raimond et al. 1981; Morganti et al. 2006). CO emission was not detected and an upper limit to the molecular gas mass of $M_{H_2} < 6.9 \times 10^6\ M_\odot$ was placed (Crocker et al. 2011). Recently, Tang et al. (2011) presented mid-infrared emission maps of the extended ionized gas, the warm molecular hydrogen, and the dust, using *Spitzer* spectroscopic observations.

In this paper, we present the deep *Chandra* observations and their imaging and spectral analysis in Sections 2–4; we summarize the observational results in Section 5, discussing the origin of the nuclear emission (Section 5.1), that of the hot gas and focusing on its peculiar central properties (Section 5.2), and the relationship between the various gas phases (Section 5.3). We finally present our conclusions in Section 6.

2. OBSERVATIONS AND DATA ANALYSIS

We utilized six archival and two new *Chandra* observations of NGC 4278, imaged with the S3 chip of the *Chandra* Advanced CCD Imaging Spectrometer (ACIS; Garmire et al. 2003). The two recent observations (PI: Fabbiano) were performed on 2010 March 15 (ObsID 11269) and 2010 March 20 (ObsID 12124), with exposure times of 81.9 ks and 25.8 ks, respectively.

We reduced and analyzed the observational data using the Chandra Interactive Analysis of Observations (CIAO) tools.[8] The CIAO script CHANDRA_REPRO was used to reprocess all data with the latest calibration, remove pixel randomization, and apply the sub-pixel ("EDSER") algorithm. We reprojected the event lists to ObsID 11269 and merged the observations to create a master event file and the associated exposure map using MERGE_ALL. After a thorough source searching with WAVDETECT (Freeman et al. 2002) using all eight co-added observations, 251 X-ray point sources were found. Details of the procedures performed to detect point sources were reported in Brassington et al. (2009) and Fabbiano et al. (2010).

From the co-added data set, *Chandra* images in 0.3–0.9 keV ("soft band"), 0.9–2.5 keV ("medium band"), and 2.5–8.0 keV ("hard band") were created and adaptively smoothed using the CIAO task *csmooth*; the smoothing kernel was constrained to yield a minimum signal-to-noise ratio of 2.5σ and a maximum of 5σ. An X-ray "false color" image was created by combining these three smoothed and exposure corrected images shown in red, green, and blue, respectively (Figures 1(a) and (b)).

To study the extended emission, we first masked out all point sources using apertures with $2''$ radii, corresponding to $\approx$95% point spread function (PSF) encircled-energy radius at 1.496 keV. The resulting "swiss cheese" image should include a minimum contribution from detected point sources. The spectral extraction was done with the CIAO script SPECEXTRACT,[9] which creates area-weighted Response Matrix Files (RMF) and Ancillary Response Files (ARF) for each region in individual observations. Background counts were taken from an annulus of source-free region between $r = 100''$ and $r = 120''$ (see Section 3.1 on determining the extent of the diffuse emission), and within the ACIS-S3 chip in all observations. For each region of interest, source spectra were grouped to a minimum of 15 counts per bin to allow spectral fitting with χ^2-statistic.

The extracted spectra were modeled with XSPEC v12.7.0, using combinations of an absorbed optically thin thermal emission (APEC model; Smith et al. 2001) and power-law components. A single line-of-sight absorption column N_{H} was used in all cases, allowed to vary freely, with the Morrison & McCammon (1983) cross-sections for the photoelectric absorption. When the fit required a very small absorption ($N_{\mathrm{H}} \ll 10^{20}$ cm^{-2}), N_{H} was frozen at the Galactic column toward NGC 4278 (1.76×10^{20} cm^{-2}; from CXC tool COLDEN[10]). Spectral modeling was done using the full 0.3–8.0 keV energy range. In the thermal APEC model, the abundance was fixed to solar, the value of the stellar population within R_e (Kuntschner et al. 2010), unless otherwise specified, and the abundance table was fixed at that of Anders & Grevesse (1989).

3. IMAGING ANALYSIS

3.1. The X-Ray Morphology

Figure 1(a) gives the $4' \times 4'$ view of the X-ray emission of NGC 4278. The bright nucleus and the point sources are clearly visible (not removed). There is extended emission in the inner $30''$, with a clear elongation along the northeast (NE; top-left) and the southwest (SW; lower right) directions. Figure 1(b)

[8] See http://cxc.harvard.edu/ciao/ for details on CIAO.
[9] See CIAO thread http://cxc.harvard.edu/ciao/ahelp/specextract/.
[10] http://cxc.harvard.edu/toolkit/colden.jsp

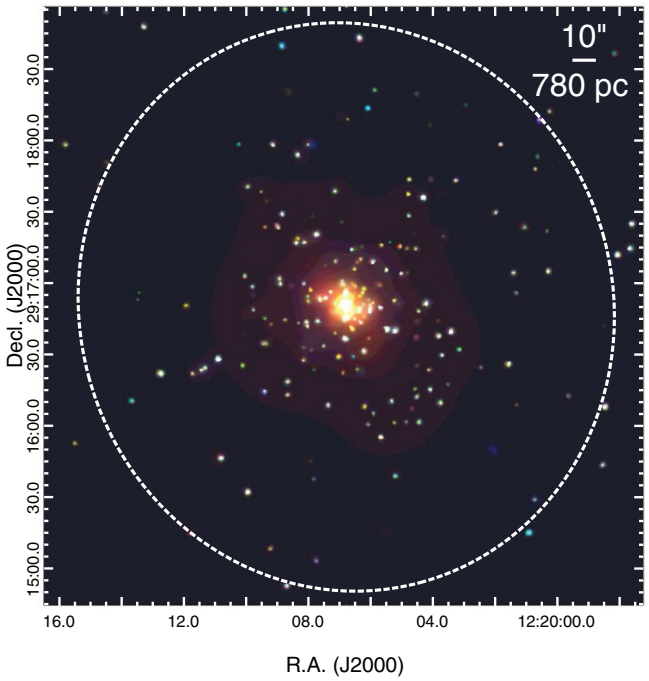

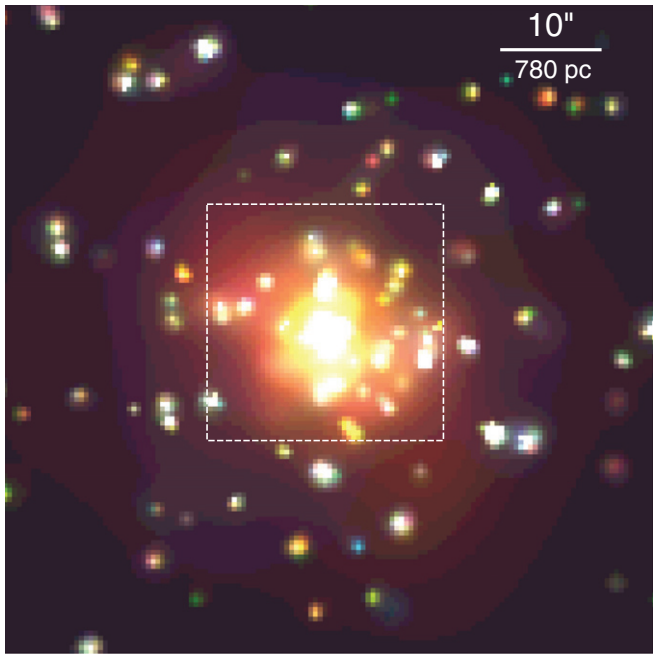

Figure 1. (Top): Three-color composite image ($4' \times 4'$) of NGC 4278. Red represents the 0.3–0.9 keV X-ray emission, green represents the 0.9–2.5 keV emission, and blue represents the 2.5–8 keV emission. North is up and east is to the left. The white dashed ellipse indicates the extent and orientation of the optical D25 ellipse. (Bottom): The zoomed-in X-ray image of the central 70″ region; the dashed square shows the region zoomed in the right panel. (Right): The innermost 20″ region showing the sub-pixel rebinned X-ray emission (0.3–2 keV; smoothed with an FWHM = 0.″3 Gaussian kernel). See Sections 2 and 3.1 for more details.

(A color version of this figure is available in the online journal.)

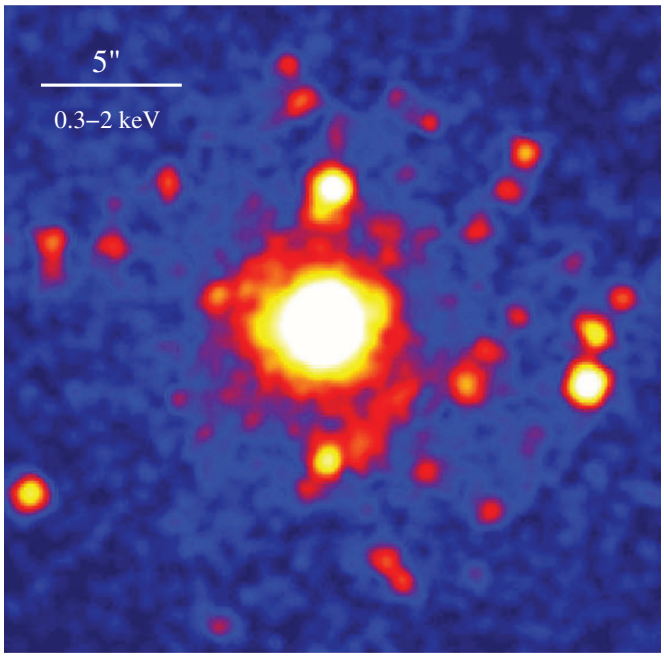

Figure 1. (Continued)

zooms-in on the central 70″ (∼5.5 kpc) region and Figure 1(c) shows the 0.3–2 keV emission in the innermost 20″ region. An extended feature is present SW of the nucleus, but not seen in other wavelengths when available images in the literature were examined.

Figure 2(a) shows the azimuthally averaged radial profile of the extended X-ray emission in the 0.3–0.9 keV energy band, which emphasizes the hot ISM presence, since harder emission mostly arises from unresolved stellar sources as binaries. We have excluded all detected sources (as explained above), and centered the concentric annuli in steps of 5″ on the nucleus, identified as the optical/IR peak. The raw profile flattens at a radius of ∼70″, where the field background starts dominating. We therefore used the 100″–140″ region to measure the local background and subtract it from the emission, to produce the net profile. We further extracted counts from every 10°-wide sector, extending from 2″ to 60″, to create an azimuthal distribution for the extended soft X-ray emission; this procedure identifies sectors that contain brighter emission (Figure 2(b)), and the results were used to guide the choice of regions for the spectral extraction (see Section 4.2).

In Figure 2(c), we show the background subtracted radial profiles of the extended emission along two directions, the NE–SW sector, which contains the X-ray brighter quadrants toward the NE (position angle, P.A. ranging between 20° and 110°, counterclockwise from N) and SW (P.A. from 180° to 290°), and the NW–SE sector, which contains the NW (P.A. from 290° to 20°) and SE (P.A. from 110° to 180°) quadrants. Along each direction, the profile is obtained as the average of the profiles over the two quadrants that compose it. The radial profiles in the optical *I* band from Cappellari et al. (2006) and in the near-IR *K* band from the Two Micron All Sky Survey (2MASS) Large Galaxy Atlas (Jarrett et al. 2003) are also shown for a comparison with the stellar light distribution. The soft X-ray profile of the NE–SW emission is clearly higher than that of the NW–SE emission within a radius $r \sim 20''$; both emissions follow the optical/IR light profile at $r > 30''$, while they are steeper than that inner of $r = 20''$. The separate brightness profiles of the brighter NE and SW quadrants closely follow each other and are not shown here; the separate profiles of the fainter NW and SE quadrants are also consistent with each other, though with lower statistics.

Having established the presence, extent, and elongation of the soft X-ray emission, we next turned to investigating the possible presence of features in the soft X-ray morphology.

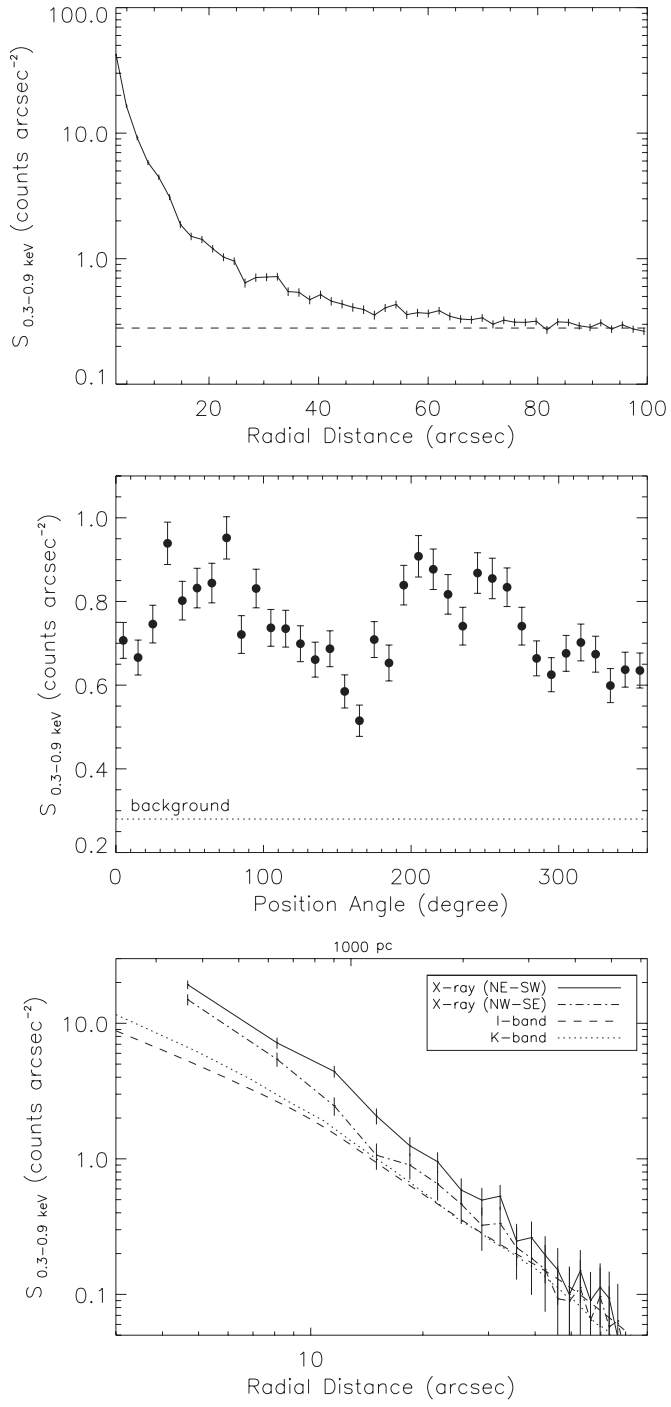

Figure 2. (Top): Azimuthally averaged radial profile of the diffuse X-ray emission (point sources masked) in the 0.3–0.9 keV band. (Middle): Average surface brightness for the extended soft X-ray emission, measured in 36 "fan-shape" sectors, each 10° wide, starting from N and moving toward E, and each one extending from a radius of 2″ (thus excluding the nucleus) out to 60″. (Bottom): Background subtracted, azimuthally averaged radial profiles in the NE–SW and the NW–SE sectors. The dashed and dotted lines are the radial profiles in the optical *I* band (Cappellari et al. 2006) and the near-IR *K* band (Jarrett et al. 2003). See Section 3.1 for more details.

We first modeled the extended soft emission within a radius of $r = 50''$ (point source removed and filled, by replacing the pixel values in the source regions with values interpolated from surrounding regions, with the tool *dmfilth*) with a smooth one-dimensional (1D) β-model using CIAO's modeling and fitting

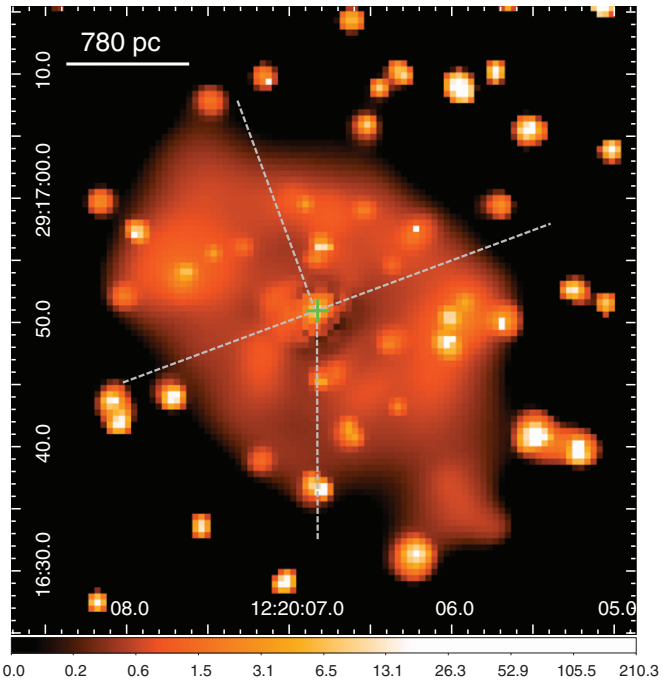

Figure 3. Intensity ratio image between the background subtracted soft X-ray emission and the 2D β-model image. The soft X-ray image was adaptively smoothed with a minimum significance of 2.5σ. The four gray lines indicate the boundaries of the quadrants defined in Section 3.1. The optical center is shown with the green cross, and the 780 pc bar (top left) is equivalent to 10″. See Section 3.1 for more details.

(A color version of this figure is available in the online journal.)

package `Sherpa`[11] (Doe et al. 2007). Clear elongation along the NE–SW direction is seen in the residual image as expected, given that the profile in this direction remains higher than that along the NW–SE (see Figure 2); thus, a 2D (elliptical) β-model was adopted. Full description of the model is available at http://cxc.harvard.edu/sherpa/ahelp/beta2d.html. The center of the model image was fixed at the location of the peak intensity of the X-ray image (x_0, y_0), and the modeling included a central point source plus a smooth extended emission, described by a 2D Lorentz model with a varying power law, known as a 2D β-model:

$$f(x, y) = A * (1 + [r(x, y)/r_0]^2)^{-\alpha}, \quad (1)$$

where $r(x, y) = \sqrt{x_1^2(1-\epsilon)^2 + y_1^2}/(1-\epsilon)$, $x_1 = (x-x_o)\cos\theta + (y-y_o)\sin\theta$ and $y_1 = (y-y_o)\cos\theta - (x-x_o)\sin\theta$, and θ is the position angle of the major axis of the ellipse. The model was blurred by a kernel representing the PSF in the image fitting.[12] The best-fit parameter values were $r_0 = 0\farcs87 \pm 0.05$ for the core radius, $\theta = 261° \pm 5°$, $\epsilon = 0.17 \pm 0.01$ for the ellipticity, and $\alpha = 1.1 \pm 0.01$. Figure 3 shows the ratio image between the background subtracted soft X-ray emission and the 2D model image (without including the bright nucleus in the model). Only features with a minimum significance of 2.5σ are shown. The point sources were retained to outline their spatial distribution with respect to the residual features. Along the NE–SW direction there are prominent clumps of emission that are likely responsible for the excess in the radial profile plots along this direction (Figures 2(b) and (c)). There is also a

[11] http://cxc.harvard.edu/sherpa4.4/
[12] See the CIAO thread http://cxc.harvard.edu/sherpa/threads/2dpsf/.

deficit of emission immediately SW of the nucleus. The overall morphology is that of an elongated elliptical shape, with an irregular distribution of clumps and deficits within it.

3.2. Comparison with Multiwavelength Maps

Figure 4 compares the contours of the extended X-ray emission in the 0.3–0.9 keV band with the *Hubble Space Telescope* (*HST*) WFPC2 *V*-band image (Carollo et al. 1997), *Spitzer* IRAC 8 μm emission (with stellar continuum removed; Tang et al. 2011), and the ionized gas maps ([O III], Hβ emission, [O III]/Hβ, EW$_{[O\,III]}$) from the SAURON survey (Sarzi et al. 2006). In each panel, we also show (1) the directions of the two-sided parsec-scale radio jet; (2) the major axis of the optical isophote and the rotation axis of the stars in the inner galactic region; and (3) the rotation axis for the ionized gas (Sarzi et al. 2006; see also Morganti et al. 2006). Note how the isophotes of the stars and of the ionized gas are oriented differently, and how the stars and ionized gas rotate about two slightly misaligned axes (Sarzi et al. 2006). The hot gas is clearly elongated but misaligned with the optical stellar body of the galaxy, and it follows more closely the ionized gas distribution and the *Spitzer* IRAC 8 μm emission.

4. SPECTRAL ANALYSIS

4.1. The X-Ray Nucleus

The X-ray emission from the nuclear source was studied by Younes et al. (2010), based on the *Chandra* pointings prior to 2010 March and on an *XMM-Newton* pointing of 2004. In their results (see their Table 2), the 0.5–8 keV flux varies from 6×10^{-13} to 1.8×10^{-12} erg cm^{-2} s^{-1}. We have examined these previous data using a different approach by directly applying the pileup model of Davis (2001), and we confirm Younes et al.'s results. We study here the nuclear emission, focusing on the new data. During the two observations acquired in 2010, the count rate was 0.06 per ACIS frame, and the photon pileup was negligible (<2%), in contrast to the high pileup fraction (∼5%–20%) when the nucleus was seen at a higher flux (Younes et al. 2010). The nucleus appears to be in its lowest flux state during the 2010 observations (Table 2).

The nuclear spectra from the last two observations were extracted from a circular aperture with a 2″ radius and were fitted jointly (Figure 5). An absorbed power-law model gave no acceptable fit (reduced $\chi^2 = 2.8$), in contrast with the highest flux state case (ObsID 4741), where a simple power law with photon index $\Gamma = 2$ could fit the nuclear spectrum. The 0.3–2 keV band shows residuals around ∼1 keV, strongly suggesting the presence of emission from hot gas. The addition of a thermal component (APEC model) takes into account these residuals in the soft band, and significantly improves the fit quality (at >99.9% confidence level, as established by the *F*-test). The best-fit temperature is $kT = 0.75 \pm 0.05$ keV and the power law $\Gamma = 2.31 \pm 0.20$. The quoted errors are 90% confidence intervals for one interesting parameter. The observed total nuclear flux is $F_{0.5-8\ \mathrm{keV}} = 1.02^{+0.11}_{-0.17} \times 10^{-13}$ erg cm^{-2} s^{-1}, and $F_{0.5-8\ \mathrm{keV}} = 1.1 \pm 0.2 \times 10^{-13}$ erg cm^{-2} s^{-1} after correction for absorption ($N_{\mathrm{H}} = 4.18 \pm 3.13 \times 10^{20}$). We also attempted to fit the two observations individually, and found $F_{0.5-8\ \mathrm{keV}} = 1.17 \pm 0.05 \times 10^{-13}$ erg cm^{-2} s^{-1} for ObsID 11269 and $F_{0.5-8\ \mathrm{keV}} = 0.95 \pm 0.08 \times 10^{-13}$ erg cm^{-2} s^{-1} for ObsID 12124 (both absorption corrected); the nuclear flux is slightly lower in the latter observation. In any case, the flux was a factor of 18 lower than the highest *Chandra* flux reported in Younes et al. (2010). The nuclear luminosity due to the power-law component is $L_{0.5-8\,\mathrm{keV}} = 2.5 \times 10^{39}$ erg s^{-1}; Table 3 gives the luminosities of the thermal and power-law components in various bands, for the last two observations fitted jointly. The comparison with the Younes et al. (2010) results is summarized

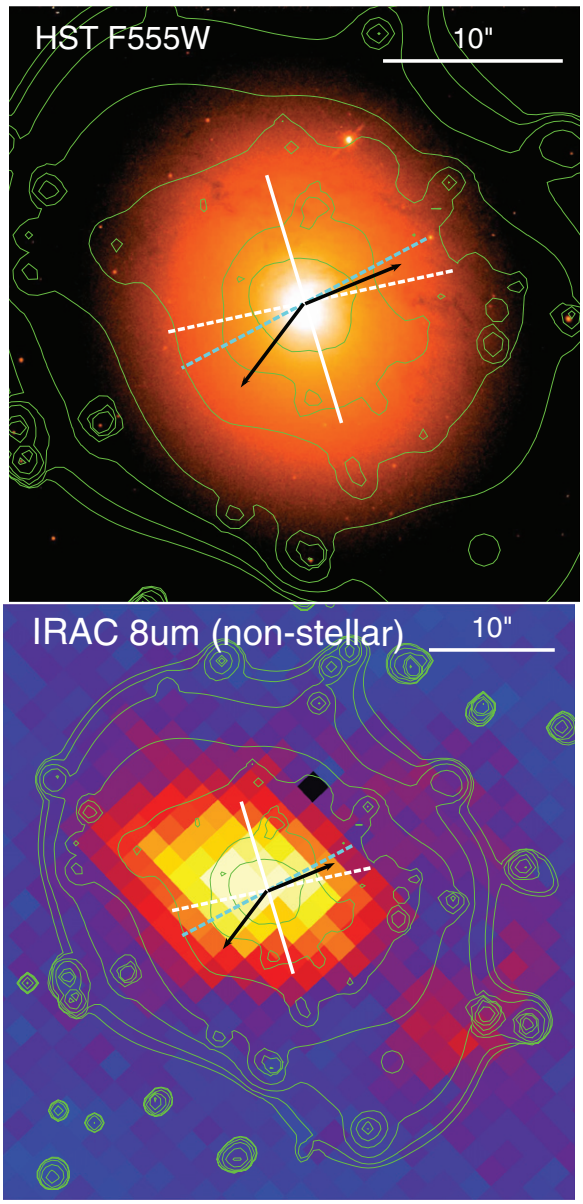

Figure 4. Contours of the extended X-ray emission in the 0.3–0.9 keV band overlaid on (top) the *HST* WFPC2 *V*-band image (Carollo et al. 1997); (bottom) the *Spitzer* IRAC 8 μm emission (with stellar continuum removed; see Tang et al. 2011). Note that the *HST* image has a smaller field of view. Relevant position angles are shown: the current radio jet directions (black arrows, from the knots S1 and N2 in the high-resolution radio map of Giroletti et al. 2005), the major axis of the optical light distribution in the inner galactic region (P.A.$_{\mathrm{phot}}$ = 16.°7; Cappellari et al. 2007, white solid line), and the rotation axis of the stars in the inner galactic region (a line perpendicular to the kinematic P.A.$_{\mathrm{kin}}$ = 12.°0, white dashed line; Cappellari et al. 2007); the rotation axis for the ionized gas (cyan dashed line; Sarzi et al. 2006). On the next page: contours of the extended X-ray emission in the 0.3–0.9 keV band overlaid on the ionized gas maps from the SAURON survey (Sarzi et al. 2006); top left: [O III] flux; top right: Hβ flux; bottom left: [O III]/Hβ; bottom right: EW$_{[O\,III]}$). The hot gas is elongated in a direction more aligned with the ionized gas distribution and the *Spitzer* IRAC 8 μm emission than with the optical stellar body of the galaxy. See Section 3.2 for more details.

(A color version of this figure is available in the online journal.)

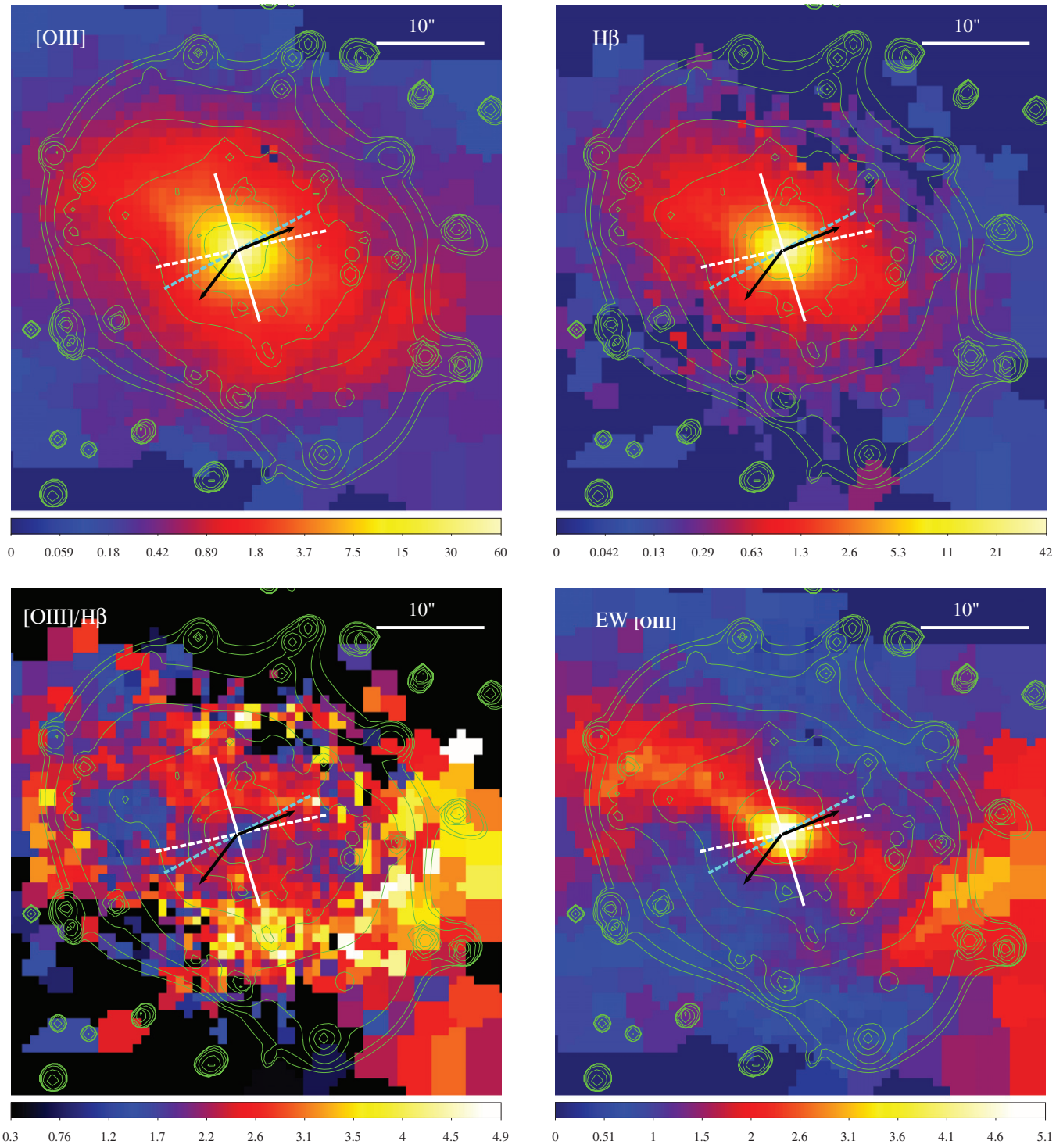

Figure 4. (Continued)

in Table 2, where the fluxes and luminosities refer to the total emission within the central 2″ radius; Figure 6 shows the luminosity variations in the 0.5–8 keV band, in Eddington units, since 2004. No significant evidence for nuclear flux variability on short timescales, within the two individual *Chandra* observations during 2010, has been found. Also, the light curves for the *Chandra* pointings prior to 2010 did not show short timescale (minutes to hours) variability, while during the *XMM-Newton* observation a 10% flux increase was found on a timescale of a few hours (Younes et al. 2010).

The thermal component alone has $L_{0.5-2\ \mathrm{keV}} = 9.9 \times 10^{38}$ erg s^{-1} and accounts for 40% of the total 0.5–2 keV emission within the $R = 2''$ region ($L_{0.5-2\ \mathrm{keV}} = 2.5 \times 10^{39}$ erg s^{-1}; Table 3). We can rule out the possibility that a significant fraction of the thermal emission at the position of the nucleus originated from the combined contribution from the AB+CV stellar population (e.g., Boroson et al. 2011; see also Section 4.2 below), since the latter is estimated to account for only ∼0.5% of the 0.5–2 keV hot gas emission in the extraction region. This estimate is based on the 2MASS *K*-band image, which gives a

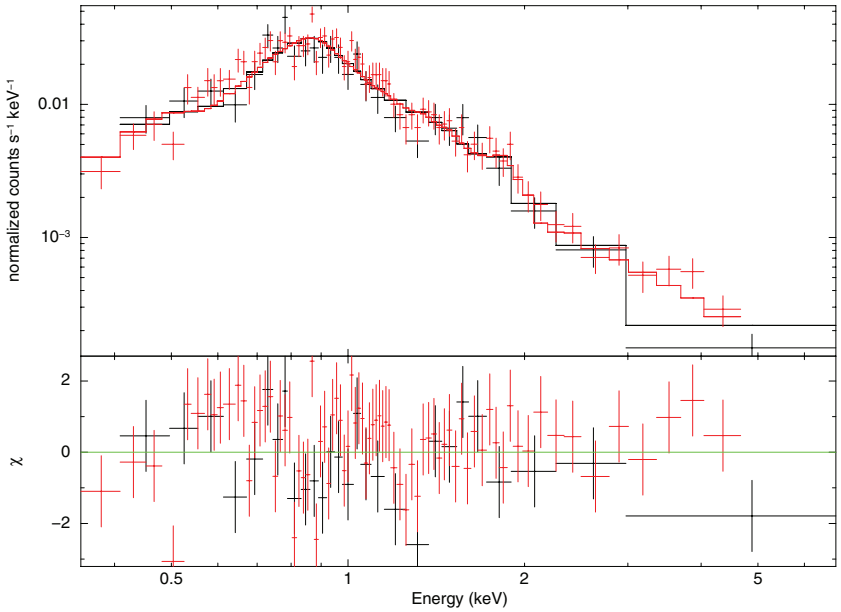

Figure 5. Best-fit spectrum of the nuclear emission using the last two observations of 2010 March (Table 2) that are not affected by pileup. The red and black lines correspond to the nuclear spectra from ObsIDs 11269 and 12124, respectively. See Section 4.1 for more details.

(A color version of this figure is available in the online journal.)

Table 2
Summary of Nuclear Variations

ObsID	Date	Γ	$F_{0.5-8\,\mathrm{keV}}$	$L_{0.5-8\,\mathrm{keV}}$
XMM-Newton	2004 May 23	2.05 [2.03–2.07]	33.8 [32.8–34.2]	10.70 [10.61–10.80]
Chandra 4741	2005 Feb 2	2.13 [2.00–2.28]	18.1 [17.1–18.8]	5.74 [5.65–6.24]
Chandra 7077	2006 Mar 16	2.26 [2.16–2.39]	7.8 [7.5–7.9]	2.55 [2.48–2.79]
Chandra 7078	2006 Jul 25	2.34 [2.22–2.47]	16.0 [14.9–16.2]	5.12 [4.99–5.74]
Chandra 7079	2006 Oct 24	2.38 [2.28–2.50]	14.1 [13.3–14.3]	4.67 [4.56–5.09]
Chandra 7081	2007 Feb 20	2.12 [2.00–2.25]	6.2 [5.9–6.4]	1.99 [1.92–2.20]
Chandra 7080	2007 Apr 20	2.02 [1.84–2.20]	5.9 [5.5–6.1]	1.86 [1.77–2.11]
Chandra 11269	2010 Mar 15	2.31 [2.11,2.51]	1.09 [0.98–1.15]	0.36 [0.35–0.38]
Chandra 12124	2010 Mar 20	2.31 [2.11,2.51]	0.94 [0.65–1.01]	0.29 [0.27–0.32]

Notes. Γ is the photon index of the nuclear power-law component; $F_{0.5-8\,\mathrm{keV}}$ is the observed flux in units of 10^{-13} erg cm^{-2} s^{-1}; $L_{0.5-8\,\mathrm{keV}}$ is the intrinsic luminosity in units of 10^{40} erg s^{-1}. Fluxes and luminosities refer to the total emission from the nuclear region ($R = 2''$). Compiled from measurements in Younes et al. (2010) and this work.

Table 3
X-Ray Spectral Properties of the Nuclear Region ($R = 2''$) from the 2010 *Chandra* Observations

N_{H} (cm^{-2})	kT (keV)	Γ	$L_{0.5-8\mathrm{keV}}$ (erg s^{-1})	$L_{\mathrm{APEC},0.5-8\,\mathrm{keV}}$ (erg s^{-1})	$L_{\mathrm{POW},0.5-8\,\mathrm{keV}}$ (erg s^{-1})	$L_{0.5-2\,\mathrm{keV}}$ (erg s^{-1})	$L_{2-10\,\mathrm{keV}}$ (erg s^{-1})
4.18 ± 3.13	0.75 ± 0.05	2.31 ± 0.20	3.5E+39	1.0E+39	2.5E+39	2.5E+39	1.1E+39

Notes. Spectral results for the 2010 *Chandra* pointings fitted jointly. Luminosities are corrected for an absorption column of $N_{\mathrm{H}} = 4.18 \times 10^{20}$ cm^{-2}; they refer to the total emission in the given band, when the spectral component is not specified. See Section 4.1. for more details.

K-band luminosity of $1.0 \times 10^9\ L_{K,\odot}$ for the region used for the extraction of the nuclear spectrum (for $M_{K,\odot} = 3.3$ mag). Adopting the $L_{0.5-2\,\mathrm{keV}}/L_K = 4.4 \times 10^{27}$ erg s$^{-1}/L_{K,\odot}$ conversion relation for the AB+CV emission (Equation (A1) in Boroson et al. 2011), this gives a stellar AB+CV luminosity of $L_{0.5-2\,\mathrm{keV}} = 4 \times 10^{36}$ erg s^{-1}.

4.2. The Extended Emission

We derived the temperature and density profiles of the hot gas using all available *Chandra* ObsIDs. In order to obtain enough counts, we analyzed the combined spectra extracted from radial bins along two directions, the NE–SW and the NW–SE sectors defined in Section 3.1. The sectors were divided in consecutive annular regions, centered at the nucleus, and selected to have ∼1000 (background subtracted) counts in the spectra (inner-to-outer radii given in Table 4). The temperature and density of the innermost $2''$ radius region were derived using the last two ObsIDs (11269, 12124) together, to avoid contamination from the nucleus as much as possible.

In addition to the sky background, it is necessary to account for the stellar contribution to the X-ray emission. The unresolved AB+CV emission (Boroson et al. 2011; Li et al. 2011b) is

Table 4
Best-fit Parameters for the Spectral Modeling with Deprojection

Annuli (arcsec)	N_H (10^{20} cm^{-2})	kT (keV)	Norm$_{kT}$	Γ	Norm$_\Gamma$
		Nucleus (ObsIDs 11269, 12124)	(χ^2/dof = 124.8/101)		
0–2	4.18 ± 3.13	0.75 ± 0.05	1.1E−5 ± 1.3E−6	2.31 ± 0.20	2.1E−5 ± 3.4E−6
		NE–SW (All ObsIDs)	(χ^2/dof = 692.8/616)		
2–4	1.76	0.61(−0.05, +0.05)	3.5E−6 ± 3.6E−7	1.8	4.5E−6 ± 4.1E−7
4–10	1.76	0.24(−0.05, +0.04)	2.5E−6 ± 6.0E−7	1.8	1.6E−6 ± 3.3E−7
10–16	1.76	0.31(−0.03, +0.04)	4.0E−6 ± 6.8E−7	1.8	1.5E−6 ± 4.3E−7
16–26	1.76	0.31(−0.04, +0.05)	3.6E−6 ± 7.6E−7	1.8	2.0E−6 ± 5.5E−7
26–40	1.76	0.18(−0.10, +0.07)	3.0E−6 ± 1.4E−6	1.8	2.3E−6 ± 6.9E−7
40–58	1.76	0.25(−0.03, +0.04)	5.1E−6 ± 1.2E−6	1.8	2.1E−6 ± 8.3E−7
		NW–SE (All ObsIDs)	(χ^2/dof = 409.5/350)		
2–4	1.76	0.76(−0.07, +0.06)	3.0E−6 ± 3.9E−7	1.8	3.8E−6 ± 4.6E−7
4–10	1.76	0.33(−0.03, +0.05)	3.3E − 6 ± 6.0E−7	1.8	3.2E−6 ± 4.0E−7
10–24	1.76	0.25(−0.05, +0.07)	2.1E − 6 ± 7.1E−7	1.8	3.3E−6 ± 5.2E−7
24–44	1.76	0.34(−0.04, +0.07)	3.3E − 6 ± 7.2E−7	1.8	3.0E−6 ± 7.1E−7

Notes. Outside the nucleus, the fit required a very small absorption column ($N_H < 10^{20}$ cm^{-2}), thus N_H was fixed at the line-of-sight Galactic value toward NGC 4278 ($N_H = 1.76 \times 10^{20}$ cm^{-2}, from the CXC tool COLDEN); also, the power-law Γ was fixed at 1.8 to account for unresolved LMXBs. Solar abundance was assumed for the thermal component in all fits. Only one χ^2/dof is given for the series of annuli in each direction, because the spectral fitting was done simultaneously for the annuli.

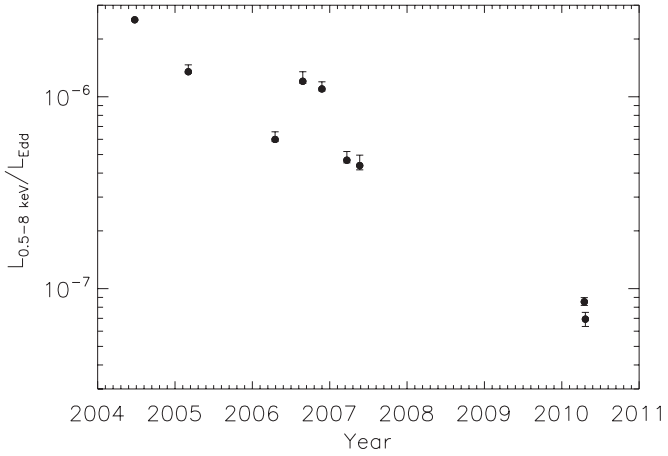

Figure 6. Variation of the Eddington ratio in the 0.5–8 keV band, for the total nuclear flux measurements from 2004 to 2010 in Table 2.

described by the spectral model derived for M32, normalized by scaling it to the K-band light enclosed within the spectral extraction regions. This AB+CV model is characterized by a combination of two thermal plasma emission components, with solar abundance and fixed temperatures of 0.4 keV and 4.6 keV, which are dominated by the emission of ABs and CVs, respectively (see Li et al. 2011b for details). An additional power-law component, with a photon index of $\Gamma = 1.8$ and a normalization free to vary, is adopted to account for the residual contribution from low-mass X-ray binaries (LMXBs; e.g., Kim et al. 2009). To account for PSF scattering of the nuclear emission, the best-fit nuclear spectrum was included as a model component, with a scaling factor fixed to the PSF wing fraction (as determined from ChaRT and MARX simulations) in the spectral extraction region; this component is negligible ($\ll$1%) in all regions except the first annulus. We finally characterize the diffuse gas with an APEC model component, with solar metal abundance. Before fitting, to account for the fact that only a fraction of the area is covered due to source removal, the ARFs generated for the annular regions were rescaled according to the missing area from source masking.

First we analyzed, using the four-component model above, the spectrum of a region covering all annuli and excluding the innermost circle of 2″ radius where the AGN dominates.[13] The best-fit temperature of the hot gas was $kT = 0.30 \pm 0.01$ keV, for χ^2/dof = 1.16. The contribution of the unresolved LMXBs was $L_{0.5-8\ keV} = 1.5 \times 10^{39}$ erg s^{-1}, close to that expected for an average shape of their X-ray luminosity function, and scaling[14] from the luminosity of detected LMXBs (Kim et al. 2009). The AB+CV contribution was fixed at $L_{0.5-8\ keV} = 2.7 \times 10^{38}$ erg s^{-1}, as derived by scaling from $L_K = 2.9 \times 10^{10}\ L_{K,\odot}$. A plot showing the best-fit model and the contribution of the various components is in Figure 7.

Next we performed spectral analysis including the nuclear region, and then accounting for the PSF scattering of the nuclear emission, and the deprojection. Assuming spherical geometry, we used the PROJCT model in XSPEC to perform the spectral deprojection. Applying spherical deprojection seems to be a reasonable approximation: the hot gas distribution is typically roundish in elliptical galaxies, and NGC 4278 has a very small optical eccentricity, and a small X-ray flattening. The resulting best-fit spectral parameters along the NE–SW and NW–SE directions are summarized in Table 4. The temperature is consistent with the 0.32 ± 0.02 keV value reported in Boroson et al. (2011) at the outer radii, but considerably hotter in the nuclear region and in the first annulus (2″–4″), in all directions

[13] Note that a one-component fit (gas only) of this region is not acceptable, even with free abundance, due to clear excess residuals at energies >1.5 keV; this holds for both the whole region and the annuli. For example, the spectrum of a circle of radius 30″, with all point sources and the AGN removed, at the best fit has $Z = 0.05\ Z_\odot$ and $kT = 0.65$ keV, with χ^2/dof = 71/50.

[14] For an average luminosity function $dN/d\ln(L_X) \propto L_X^{-0.5}$ (Kim et al. 2006, 2009), and for an observed total $L_{0.5-8\ keV} = 4.5 \times 10^{39}$ erg s^{-1} for the LMXBs with L_X in the range 10^{37}–10^{38} erg s^{-1} (that are all detected), one derives a total $L_{0.5-8\ keV} = 1.4 \times 10^{39}$ erg s^{-1} for the LMXBs with L_X in the range 10^{36}–10^{37} erg s^{-1}; after subtracting the contribution of the detected LMXBs in this range, the unresolved emission is $L_{0.5-8\ keV} = 1.3 \times 10^{39}$ erg s^{-1}.

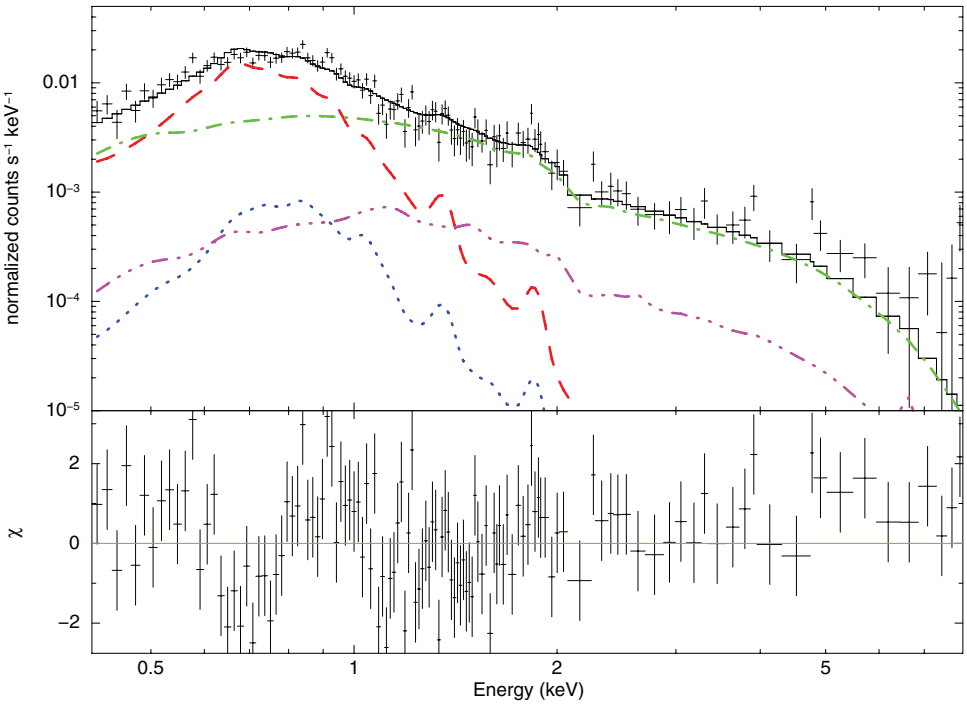

Figure 7. Spectrum and its best-fit (black solid line) for the total diffuse emission, excluding the central AGN region. The contributing components are also shown: the hot gas (red dashed line), the unresolved LMXBs (green dash-dotted line), the unresolved AB+CV stars, using M32 as a template for the normalization (blue dotted and magenta dash-dotted lines). See Section 4.2 for more details.

(A color version of this figure is available in the online journal.)

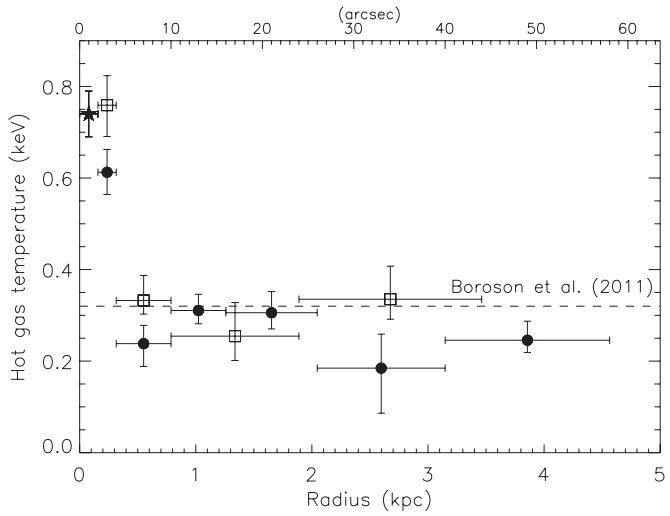

Figure 8. Radial distribution of gas temperature derived from spectral deprojection along two directions (NE–SW, filled circles and NW–SE, open boxes). The temperature for the inner 2″ derived using only the last two observations is marked by a star. See Section 4.2 for more details.

(Figure 8). Note that the spectral fitting of the same annular regions without deprojection gives a temperature profile, out of the nuclear region, consistent with the deprojected one, within the errors. The inner hot component is also found again at a significant level, thus it is not due to artifacts of deprojection or of the *projct* model; the deprojected temperature at the center ($kT = 0.75$ keV) is higher by 14% than the projected value. Finally, the sum of the luminosities of the unresolved LMXBs in each annulus is consistent with the luminosity of this component found for the whole region (see above); the same is true by construction (i.e., the scaling from L_K) for the sum of the AB+CV emission in all annuli.

Given the peculiar and unusual result of a significantly hotter thermal emission at the nucleus and in the surrounding 2″–4″ annulus, we next investigated whether the high temperature is a real feature of the hot gas, or if it could be due to an underestimate of the nuclear contribution. We focus on ObsID 11269 because of its depth and well-characterized nuclear emission (pileup free) in a single observation. We performed ChaRT+MARX simulations and found that the PSF wing may scatter 2% of the nuclear APEC component to the 2″–4″ radial bin (or a 0.5–2 keV flux of $6.0 \pm 1.2 \times 10^{-16}$ erg cm^{-2} s^{-1}). The flux of the thermal component is 9×10^{-15} erg cm^{-2} s^{-1}, which requires the PSF scattering fraction of the nuclear emission to be unrealistically underestimated (30% instead of 2%). Moreover, the contribution from unresolved stellar sources is an order of magnitude lower than the APEC component. Thus, we conclude that the hot thermal component is significant and arises from gas at a higher temperature in the inner few hundreds pc.

The deprojected density in each spherical shell is shown in Figure 9. Densities, along with other physical properties of interest for the hot gas, are presented in Table 5. We accounted for the fact that only a fraction of the area within a given annulus was covered, due to source removal. The electron number density n_e of the hot gas was derived from the emission measure ($\int n_e^2 dV$) of the APEC component of each extraction region. This produces the average number density along each direction (NE–SW or NW–SE) because the spectra of corresponding annuli, at the same radial distance, for each couple of quadrants in a given direction, were combined in the fit. Assuming spherical symmetry, the volume covered by the quadrants was properly calculated using their apex angle. The actual 3D geometry and topology of the hot gas may have an effect on the derived density and temperature profiles.

Table 5
Derived Physical Parameters for the Hot Gas Component

Annuli (arcsec)	n_e (cm^{-3})	p (dyn cm^{-2})	E_{th} (erg)	L_{apec} (erg s^{-1})	M_{hot} ($10^5\ M_\odot$)
			Nucleus (ObsIDs 11269, 12124)		
0–2	0.242 ± 0.030	5.8E−10	4.1E+53	1.0E+39	1.0
			NE–SW (All ObsIDs)		
2–4	0.072 ± 0.008	1.4E−10	4.0E+53	1.6E+38	1.1
4–10	0.019 ± 0.005	1.5E−11	6.9E+53	3.5E+38	5.0
10–16	0.011 ± 0.002	1.1E−11	1.7E+54	1.7E+38	9.6
16–26	0.005 ± 0.001	4.7E−12	3.1E+54	1.2E+38	18.0
26–40	0.002 ± 0.001	1.4E−12	3.2E+54	8.5E+37	30.3
40–58	0.002 ± 0.001	1.4E−12	9.2E+54	8.4E+37	65.5
			NW–SE (All ObsIDs)		
2–4	0.073 ± 0.009	1.8E−10	4.0E+53	9.7E+37	0.9
4–10	0.023 ± 0.004	2.4E−11	9.1E+53	1.9E+38	4.8
10–24	0.004 ± 0.001	3.6E−12	1.8E+54	8.7E+37	12.6
24–44	0.002 ± 0.001	2.3E−12	6.7E+54	6.8E+37	35.0

Notes. The electron number densities were derived from the emission measure for the thermal component. Luminosities are reported for the 0.5–8 keV range and are absorption corrected ($N_H = 1.76 \times 10^{20}$ cm^{-2}).

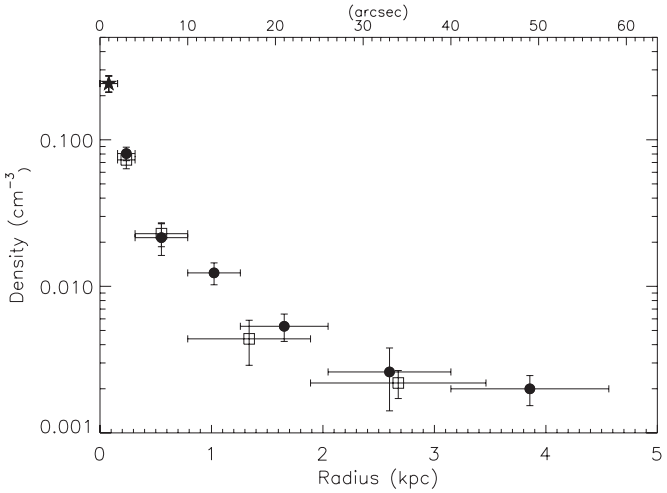

Figure 9. Radial distribution of gas density derived from spectral deprojection along two directions (NE–SW, filled circles and NW–SE, open boxes). The density for the inner 2″ derived using only the last two observations is marked by a star. See Section 4.2 for more details.

Here, the hot gas shows some clumpiness (Section 3.1), but it is not dominated by it (e.g., there are no true "holes"). With the available counting statistics, a more refined analysis that measures the separate properties of the excesses/deficits and of the remaining regions is not allowed. However, one should not expect significantly different results from when a smooth gas distribution is assumed, since overall the distribution of excesses/deficits is rather homogeneous.

Finally we investigated the extent of the uncertainties that the abundance fixed at the solar value introduces on the values derived for the radial temperature and density profiles. For the same spectral model used above, if Z is left free for the hot gas, at the best fit it is unreasonably low ($Z = 0.09^{+0.03}_{-0.02}\ Z_\odot$); the temperature slightly increases, by <10% in all regions, and the density increases[15] by a factor of ∼3. For Z in the range of $0.5 < Z/Z_\odot < 2$, which is more plausible and as obtained from the more accurate analysis possible for the hot gas-rich galaxies (e.g., Humphrey & Buote 2006), kT changes within 10%, and the density decreases by 30% ($Z = 2\ Z_\odot$) or increases by 40% ($Z = 0.5\ Z_\odot$), with respect to the best-fit values for $Z = Z_\odot$.

Iron enrichment from Type Ia supernova (SNIa) explosions is expected to increase the iron abundance Z_{Fe} of the hot gas with respect to that of the stellar population from which it originates; in order to let Z_{Fe} free to vary, we made a test with the variable abundance plasma model VAPEC. If all elements vary independently, and their abundance is the same in all regions, Z_{Fe} is not constrained ($Z_{Fe} = 1.01^{+4.54}_{-0.56}\ Z_{Fe,\odot}$). If all the elements other than iron are arbitrarily[16] fixed at the solar abundance, then $Z_{Fe} = 0.4 \pm 0.12\ Z_{Fe,\odot}$; the temperature is larger by 10% and the density by 20%, with respect to the $Z_{Fe} = Z_{Fe,\odot}$ case. Fixing $Z_{Fe} = 2\ Z_{Fe,\odot}$, as a test value in case of efficient SNIa enrichment, the best-fit kT is lower by 10% and the density by 20%. All in all, these Z_{Fe} variations correspond to minor changes in the radial temperature and density profiles.

In recent *Chandra* studies of hot gas-poor galaxies such as NGC 4278, but with much lower typical exposures, the abundance was not well constrained. Complex emission models were not statistically required, and the measured abundance was model dependent: a one-component modeling with low abundance could reproduce the data as a two-temperature modeling with abundances close to solar (e.g., Kim & Fabbiano 2003; Humphrey & Buote 2006). Here, thanks to the exceptionally deep exposure, we could establish the presence of more than one spectral component; but even when including all the components from the stellar population, the best-fit Z is lower than expected. However, it is well known that abundance measurements through X-ray spectral fitting are problematic and can only give a lower limit to the true abundance (e.g., Kim 2012 and references therein). In general, Z (and Z_{Fe} as well) depends on the number of spectral components in the fitting and are larger when more components are allowed (which applies to gas-poor galaxies with a relatively more important stellar

[15] Very similar results are obtained using a two-component spectral model, accounting only for hot gas and unresolved LMXBs.

[16] Oxygen is often sub-solar and Ni is often super-solar in several galaxies (e.g., Kim 2012).

contribution, to multi-temperature gas, and to undetected temperature variations; e.g., Kim et al. 1996; Buote & Fabian 1998; Baldi et al. 2006). Thus, even when the abundance is formally "constrained" by the fitting, the actual result is a lower limit. Given these uncertainties, we find no reason to adopt an abundance much lower than solar, which is the value for the stellar population that produces the hot gas (Kuntschner et al. 2010); we have shown, though, that even if Z or $Z_{\rm Fe}$ were to be in the range between 0.5 and 2 of the solar values, the changes in the radial temperature and density profiles would be minor.

5. SUMMARY OF THE OBSERVATIONAL RESULTS AND DISCUSSION

A deep (579 ks) *Chandra* observation of the elliptical galaxy NGC 4278, including two pointings during year 2010 and six pointings prior to 2010, has been analyzed. The main results are as follows.

1. The nuclear emission dominates the X-ray image, but its 0.5–8 keV flux in 2010 was the lowest among all pointings, and ∼18 times lower than at its brightest state seen with *Chandra* (in 2005). At the nucleus, within $r = 2'' = 156$ pc, a power-law spectral component (with $\Gamma = 2.31 \pm 0.20$) and a thermal component (with $kT = 0.75 \pm 0.05$ keV) coexist with an average $L_{0.5-8\,\rm keV} = 2.5 \times 10^{39}$ erg s^{-1} during year 2010 and with $L_{0.5-8\,\rm keV} = 1.0 \times 10^{39}$ erg s^{-1}, respectively.
2. After merging data from all pointings, hot gas is detected out to a radius of ∼5 kpc, with a total $L_{0.5-8\,\rm keV} = 2.4 \times 10^{39}$ erg s^{-1}. On the galactic scale, the hot gas shows an elliptical shape, elongated in the NE–SW direction; its distribution is clearly different from that of the stellar component of the galaxy, having a flatter shape and a different orientation. The hot gas seems to follow the distribution of the ionized gas, which resides in a rotating, inner disk, and of the warm dust emission detected with *Spitzer*.
3. The image ratio with the best-fit 2D modeling of the surface brightness (i.e., unsharp masking; Figure 3) shows that the gas distribution surrounding the bright nucleus is not smooth, but includes regions where the brightness is lower than average, and various clumps. In particular, two larger clumps are present NE and SW of the nucleus, at a distance of ∼10″. These regions of enhancement of the brightness are not likely to be concentrations of stellar sources, being clearly extended; spectral analysis of the diffuse emission also indicates thermal emission from hot gas, and not from fainter LMXBs.
4. The temperature and density profiles derived from deprojection along the NE–SW and NW–SE directions are consistent with each other at all radii, except for the temperature in the annulus surrounding the nucleus, which is lower in the direction of the elongation (NE–SW). The hot gas temperature stays at 0.6–0.8 keV out to a radius of ∼300 pc, and drops sharply to ∼0.3 keV outside, keeping a constant (or slowly decreasing) value out to ∼5 kpc. The density profile shows a smooth decrease throughout the region examined.

The above results prompt the following questions. What is the origin of the nuclear emission and of the hotter gas at the galactic center? What produces the hot gas elongation? Is there a relationship between the hot and the warm gas that seems to follow the same projected distribution? Taking also advantage of the information at the radio wavelengths, we now investigate the hot gas origin and evolution, and the activity cycle, in this medium-mass elliptical galaxy; systems of this mass have not been investigated in such detail previously. We examine in turn the origin of the nuclear emission in Section 5.1, that of the central hot gas in Section 5.2, and the relationship between the hot, warm, and cold gas phases in Section 5.3.

5.1. The Nuclear Emission

The X-ray spectral shape of the low-luminosity AGN during the most recent 2010 March pointings is consistent with that determined from pointings made between 2005 and 2007 by *Chandra* and by *XMM-Newton* in 2004 (Table 2): During these previous brighter states, the average photon index was $\Gamma = 2.2^{+0.1}_{-0.2}$, affected by small intrinsic absorption ($N_{\rm H} < 6.7 \times 10^{20}$ cm^{-2}; Younes et al. 2010). The source was brightest in 2004 and decreased by a factor of 5.7 by 2007; this trend of decrease in flux continued through 2010 (Section 4.1; Figure 6). Based on the spectral energy distribution from radio to X-rays, it was suggested that at low X-ray flux the nuclear emission is more typical of LINERs (and possibly originates in an RIAF and/or a jet), whereas at high X-ray flux it resembles more that of a Seyfert (Younes et al. 2010). The power-law component of the nucleus in 2010 had $L_{0.5-8\,\rm keV}/L_{\rm Edd} = 5.9 \times 10^{-8}$, where the Eddington luminosity $L_{\rm Edd} = 4.25 \times 10^{46}$ erg s^{-1} for the MBH mass in Table 1. The bolometric correction ($L_{\rm bol}/L_X$) for low-luminosity AGNs is believed to be lower than the value of standard AGNs (∼30, Elvis et al. 1994), where the accretion disk dominates the emission; for example, Ho (2009) suggested that $L_{\rm bol}/L_{2-10\,\rm keV} \approx 8$ for low-luminosity AGNs, and, for a large sample including nuclei with $L_{\rm bol}/L_{\rm Edd} \lesssim 0.1$, a median $L_{\rm bol}/L_{2-10\,\rm keV} \approx 15.8$. Therefore, the AGN in NGC 4278 is a very sub-Eddington radiator (Table 3 gives the 2–10 keV nuclear luminosity), and its low luminosity could be the result of a low radiative efficiency, provided that the mass accretion rate is low. Thanks to the large dimming of the nucleus in 2010, we could derive the gas properties close to the MBH, a result used in the following to derive an estimate of the mass accretion rate, and then to discuss the accretion modalities.

For material accreting on the MBH at rate $\dot{M}$, such that $\dot{m} = \dot{M}/\dot{M}_{\rm Edd} \ll 0.01$ (where $\dot{M}_{\rm Edd} = 22\ M_{\rm BH}(10^9\ M_\odot)\ M_\odot$ yr^{-1}), the accretion flow can become an RIAF, with an efficiency for producing radiation of $\epsilon \sim 10\dot{m}$ (Narayan & Yi 1995); the expected $L_{\rm bol}$ is then $\sim 10\dot{m}\dot{M}c^2$. We can adopt for $\dot{M}$ the mass accretion rate given by the steady and spherically symmetrical Bondi (1952) solution, $\dot{M}_B$ (e.g., Loewenstein et al. 2001; Di Matteo et al. 2003; Pellegrini 2005). An accretion rate $\lesssim \dot{M}_B$ also enters in the viscous rotating analog of the Bondi treatment represented by the RIAF models (Quataert 2003; Narayan & Fabian 2011). $\dot{M}_B$ is given by $\dot{M}_B = \pi G^2 M_{\rm BH}^2(\rho_\infty/c_{s,\infty}^3)[2/((5-3\gamma)]^{(5-3\gamma)/2(\gamma-1)}$, where γ is the polytropic index ($\gamma = 1$ (isothermal) to 5/3 (adiabatic)), c_s is the sound speed, and "∞" refers to the ambient conditions (e.g., Frank et al. 2002). Ideally, one should insert into this formula the gas density and temperature at the accretion radius $r_{\rm acc} = 2\ GM_{\rm BH}/c_{s,\infty}^2$, where the dynamics of the gas start to be dominated by the potential of the MBH. In practice, one uses fiducial temperature and density for the circumnuclear region, determined as close as possible to the MBH. For the values for the nuclear region in Tables 4 and 5, one obtains $r_{\rm acc} = 15$–25 pc and $\dot{M}_B = (0.5$–$5) \times 10^{-3}\ M_\odot$ yr^{-1} (for $\gamma = 5/3 - 1$); the corresponding $\dot{m}_B = (0.7$–$7) \times 10^{-4}$ is very low, within the RIAF regime. This $\dot{M}_B$ is based on gas properties that are average for a sphere of 156 pc radius (∼6 $r_{\rm acc}$), and thus its

value should be taken with some caution; for example, this $\dot{M}_B$ may underestimate the true mass accretion rate at $r_{\rm acc}$ if the density rises steeply toward $r_{\rm acc}$ (but this seems to not be the case; see the modeling of Section 5.2.1).

Using an average $\gamma = 4/3$, then $\dot{M}_B = 2.1 \times 10^{-3}\ M_\odot\ {\rm yr}^{-1}$ and $L_{\rm bol} = 10 \dot{m}_B \dot{M}_B c^2 \sim 3.3 \times 10^{41}$ erg s^{-1} (while a standard accretion disk would have a radiative output of $L_{\rm acc} = 0.1 \dot{M}_B c^2 \sim 1.2 \times 10^{43}$ erg s^{-1}); for the whole range of $\dot{M}_B$, $L_{\rm bol} \sim$ (0.02–2) $\times 10^{42}$ erg s^{-1}. Adopting a correction factor appropriate for the spectral energy distribution of an RIAF, i.e., $L_{0.5-8\ {\rm keV}} \lesssim 0.15 L_{\rm bol}$ (Mahadevan 1997), for the average $\dot{M}_B = 2.1 \times 10^{-3}\ M_\odot\ {\rm yr}^{-1}$ one expects $L_{0.5-8\ {\rm keV}} \lesssim 5 \times 10^{40}$ erg s^{-1}, which is $\lesssim$20 times larger than the observed $L_{0.5-8\ {\rm keV}} = 2.5 \times 10^{39}$ erg s^{-1} (the expected $L_{0.5-8\ {\rm keV}} \lesssim 2.8 \times 10^{39}$ erg s^{-1} for the lowest estimate of $\dot{M}_B$, and $\lesssim 3 \times 10^{41}$ erg s^{-1} for the largest). Reductions of the mass accretion rate on the way to the MBH have often been claimed for RIAFs, since they include solutions where little of the mass available at large radii is accreted onto the MBH due to outflows or convective motions (Blandford & Begelman 1999; Stone et al. 1999; Igumenshchev et al. 2003). Another source of reduction is given by the possibility that the gas has non-negligible angular momentum beyond the Bondi radius (Proga & Begelman 2003; Narayan & Fabian 2011). The latter authors calculated the rate at which mass accretes onto an MBH from rotating gas for RIAFs in galactic nuclei, and found that $\dot{M} \sim$ (0.3–1)$\dot{M}_B$, for a plausible viscosity parameter value $\alpha = 0.1$. Large reductions of $\dot{M}$ with respect to $\dot{M}_B$ are not required here; for example, if $\dot{M} \sim 0.3 \dot{M}_B$, accounting only for the effect of rotation, then $L_{\rm bol}$ would decrease by a factor of $\sim$10, and the predicted $L_{0.5-8\ {\rm keV}}$ for the average $\dot{M}_B$ would be $\lesssim 5 \times 10^{39}$ erg s^{-1}, close to that observed. The largest possible reduction in $\dot{M}_B$ still reproducing the observed luminosity is of a factor of $\sim$10 (calculated for the largest estimate of $\dot{M}_B$).

The accretion process at the nucleus of NGC 4278 has also been studied recently by modeling the radio-to-X-ray emission with an inner RIAF, an outer truncated thin accretion disk, and a jet, with the possibility of a radially varying mass accretion rate, within the RIAF region, to account for outflows (Nemmen et al. 2011). The radio was explained with a jet origin, the 100–1 μm emission required an outer accretion disk truncated at 30–100 Schwarzschild radii, and the X-rays could be equally well reproduced mostly by the RIAF (from inverse Compton scattering of synchrotron photons in the flow) or mostly by the jet (from synchrotron photons from the jet; see also Yuan & Cui 2005). The best-fit models, respectively, for the RIAF-dominated and the jet-dominated cases, have an accretion rate[17] at the outer disk of $\dot{m}_{\rm out} = 7$ or 4×10^{-4}, and an accretion rate on the MBH of $\dot{m}_{\rm in} = 4.4$ or 0.9×10^{-4}. These $\dot{m}_{\rm out}$ values are within the $\dot{m}_B$ range estimated here, and $\dot{m}_{\rm in}$ is not too different from $\dot{m}_{\rm out}$; for the case of the X-rays coming mostly from the RIAF, $\dot{m}_{\rm out} = 1.6 \dot{m}_{\rm in}$, a result similar to that found above for the small reduction (if any) of $\dot{m}_B$ to reproduce the observed $L_{0.5-8\ {\rm keV}}$. In fact, the $\dot{m}_B$ from our analysis, for $\gamma = 1.5$ as adopted by Nemmen et al., produces $L_{0.5-8\ {\rm keV}} \lesssim 1.4 \times 10^{40}$ erg s^{-1} if ending in an RIAF, and it should then be reduced by $\lesssim$2.3 times to reproduce the observed luminosity.

In conclusion, the hot gas observed with *Chandra* near the MBH has density and temperature consistent with the idea that the nuclear luminosity comes from an RIAF, with an $\dot{M}$ close to that estimated with the Bondi formula. If all the nuclear X-rays are to come from the accretion flow, $\dot{M}_B$ can be reduced by a factor expected in case of rotation, still reproducing the observed luminosity; the latter constrains the reduction to be not larger than a factor of $\sim$10. If the X-rays come mostly from a nuclear jet, the accretion flow luminosity must be lower than that observed, and then a more important reduction for $\dot{M}_B$ is allowed, as can be achieved when outflows or convection are added. A further important constraint on how much mass must be accreting is given by the total energy output from accretion, as will be discussed in Section 5.2.3.

5.2. The Origin of the Central Hotter Gas

In a galaxy the size of NGC 4278, given standard assumptions concerning SNIa heating, the mass losses from evolving stars are expected to give rise to an outflow on the galactic scale (see also Section 5.2.1 below); this agrees with the low observed hot gas content, of a few $\times 10^7\ M_\odot$ (Table 5). The intriguing central peak in temperature, instead, is a new finding, that could be produced by the following causes: (1) the MBH gravity field; (2) a nuclear outburst triggered by a past high accretion rate phase (i.e., in the AGN mode); (3) hot accretion during a quiescent, low accretion rate state; and (4) kinetic heating from the jet.

In the following, these hypotheses are examined in turn. The first one is studied with hydrodynamical simulations (Section 5.2.1); the next two are examined in light of the predictions of previous results from numerical simulations (Section 5.2.2); the last one is investigated through energetic calculations that also exploit the radio information (Section 5.2.3).

5.2.1. Hot Gas Evolution without AGN Feedback

We performed hydrodynamical simulations for the evolution of the stellar mass losses for a detailed galaxy model built for NGC 4278 without feedback from the MBH; the aim is to establish what can and cannot be explained by this basic model. The underlying three-component galaxy mass model is made by superposing a stellar and a dark distribution, *plus a central MBH*, of mass fixed to that in Table 1. All other details regarding the galaxy model and the simulations are given in the Appendix.

The resulting gas flow on the galactic scale is an outflow driven by SNIa heating during the entire evolution; a small accretion region at the center is always present, due to the cuspy mass profile, typical of elliptical galaxies (e.g., Pellegrini 2012). With time increasing, the SNIa specific heating ($L_{\rm SN}/\dot{M}_* \propto t^{0.2}$, where $L_{\rm SN}$ is the SNIa heating rate and $\dot{M}_*$ is the stellar mass-loss rate) slowly increases; this produces a decrease in the inflow velocity and of the radius of the inflowing region, that goes down to $\sim$30 pc at the present epoch. At the center, the gas density keeps decreasing and the temperature increasing with time (Figure 12 in the Appendix); mass flows through the innermost grid point (5 pc) at a decreasing rate, reaching $\dot{M} \sim 0.003\ M_\odot\ {\rm yr}^{-1}$ at the present epoch. Even though the density rises toward the center in the model, this value of $\dot{M}$ is within the range derived for $\dot{M}_B$ in Section 5.1 (at its upper end).

The temperature and density profiles at an age consistent with that of the stellar population of NGC 4278 (10.7 ± 2.14; Terlevich & Forbes 2002) are shown in Figure 10. Initially, the temperature drops toward the center, and its central value is $\sim$0.55 keV at an age of $\sim$10 Gyr; this value is an average calculated for a central sphere of radius 2″, as in the observations, and includes the contribution of a very inner region where the central MBH creates a spike in the gas injection

[17] $\dot{m}$ is the Eddington-scaled mass accretion rate.

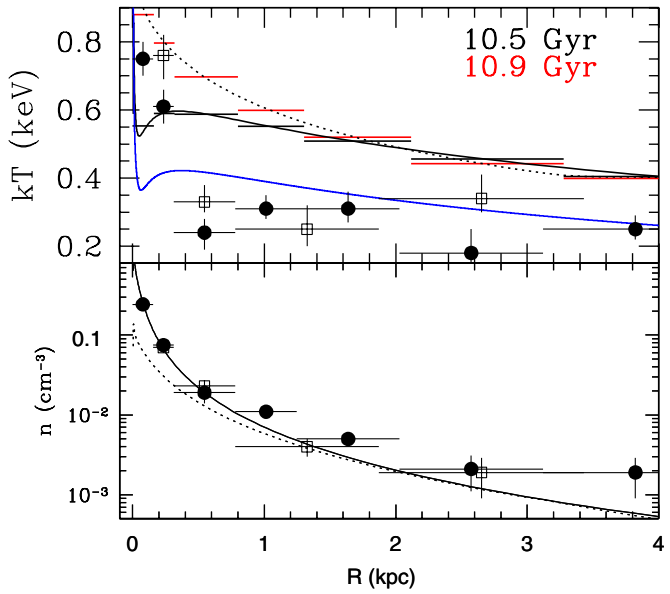

Figure 10. Three-dimensional radial temperature profile (upper panel) and density profile (lower panel) for the observed values (full circles and open squares, respectively, for the NE–SW and NW–SE quadrants), and for the representative model discussed in Section 5.2.1, at two epochs: 10.5 Gyr (solid line) and 10.9 Gyr (dotted line). The model temperature at these epochs is also shown with bars, calculated by averaging the temperature with the 0.3–8 keV emission over bins of a width as close as possible to that used for the observed data (compatibly with the spacing of the numerical grid). The blue line shows the temperature expected from the thermalization of the stellar motions, $T_\sigma(r)$; note the central spike due to the MBH. See Section 5.2.1 and the Appendix for more details.

(A color version of this figure is available in the online journal.)

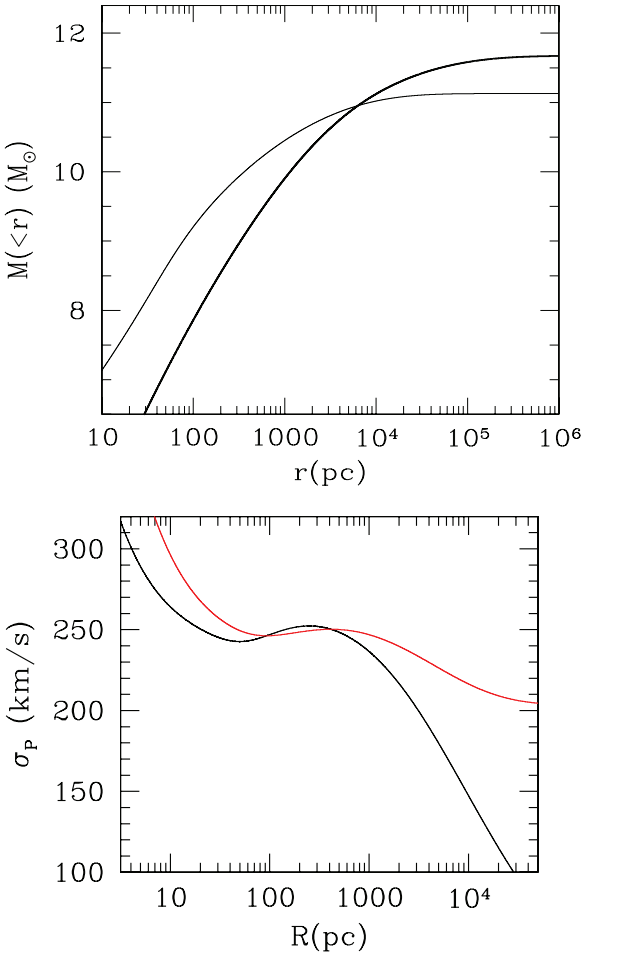

Figure 11. Top: the mass profile for the adopted galaxy model (thick line for the dark mass and thin one for the stellar mass). Bottom: the model projected stellar velocity dispersion, in black, and the aperture velocity dispersion, in red. Note how the red curve reaches the aperture velocity dispersion of 252 km s^{-1} at $R_e/8$ (and of $231 \pm 5\%$ km s^{-1} at R_e, as observed by Kuntschner et al. 2010); note also the central increase produced by the MBH.

(A color version of this figure is available in the online journal.)

temperature (see Figure 10). Later, the temperature becomes higher at the center (∼0.85 keV) and decreases smoothly out of 2″ (Figure 10, dotted line), without a sharp drop as instead observed. The model temperature is then larger than observed at the center and agrees with that observed in the surrounding annulus of radii 2″–4″ only for the NW–SE quadrant; thus, the observed temperature cannot be reproduced by the models as a long-lasting feature.[18] The model density profile is in reasonable agreement with the *Chandra* one at 10 Gyr, but it is lower than that inward of ∼400 pc for later epochs (Figure 10). The MBH clearly heats the gas in its surroundings, through the combined effects of its gravitational field, which leads to gas compression, and an increase in the stellar heating (due to the stellar velocity dispersion enhancement caused by the MBH within its sphere of influence[19]; see the Appendix and Figure 11). This heating, though, keeps the gas temperature very high on a much smaller scale than observed (Figure 10). Evidently, the gas properties close to the center are established by different (additional) phenomena with respect to those simply connected with the MBH gravity, the SNIa heating, and mass input from stellar mass losses. This analysis also shows that accretion is possible even for gas with a central temperature as high as observed.

Another result of this investigation is that, outward of a ∼0.5 kpc radius, the observed temperature is lower than in the model and consistent just with the temperature expected from the thermalization of the stellar motions (T_σ; Figure 10). Note that the stellar heating could be lowered by at most ∼20% for different mass models still consistent with the observational constraints. When coupled with the fact that the model density also tends to be lower than observed outside ∼1 kpc, possibly indicating too much degassing, all these could point to a lower efficiency of the SNIa energy mixing process than standardly adopted. In fact the fraction of the SNIa kinetic energy that is turned into heat is uncertain, and may depend on the environment surrounding the expanding supernova remnants (e.g., Tang et al. 2009; Pellegrini 2011). In massive, hot gas-rich early-type galaxies, the SNIa bubbles should disrupt and share their energy with the local gas within $\sim 3 \times 10^6$ yr (Mathews 1990); in less massive spheroids in a global wind, instead, 3D hydrodynamical simulations of discrete heating from SNIa suggest a non-uniform thermalization of the SNIa energy, with overheated gas advected outward, carrying a large fraction of the SNIa energy with it (Tang et al. 2009). Unfortunately, additional information on the mixing of the SNIa ejecta cannot be derived from measurements of the iron abundance $Z_{\rm Fe}$ of the hot gas, as discussed in Section 4.2. Another possibility is that the gas is cooled by the presence of other colder phases in the ISM (see Section 5.3).

[18] A temperature profile within ∼400 pc similar to the one observed is produced between the two epochs shown in Figure 10, but for a very brief time, lasting $\lesssim 10^7$ yr.

[19] The sphere of influence of the MBH has a radius of $r_{\rm BH} = GM_{\rm BH}/\sigma_0^2 = 23$ pc for the $M_{\rm BH}$ and central stellar velocity dispersion σ_0 values in Table 1.

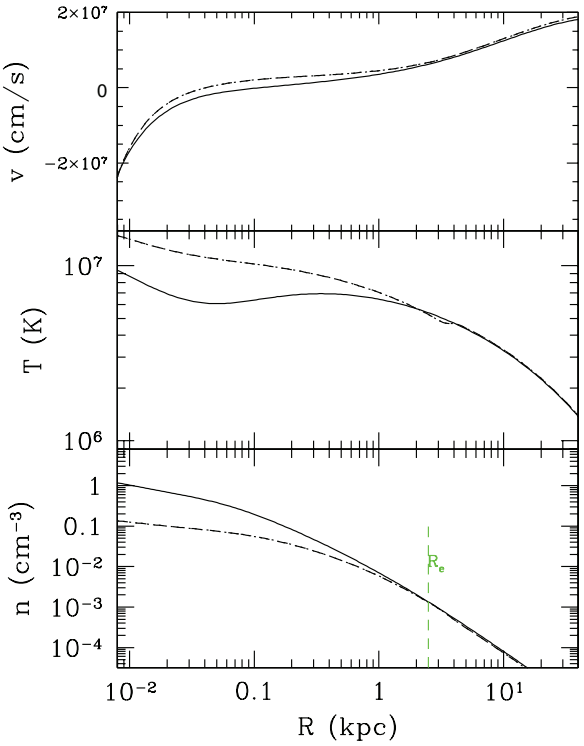

Figure 12. Radial trend of the main hydrodynamical quantities of the gas flow for the representative model described in the Appendix and discussed in Section 5.2.1; displayed are the velocity (negative inward), top; the temperature, middle; the gas number density, bottom; for a galaxy age of 10.5 (solid) and 10.9 (dot-dashed) Gyr.

(A color version of this figure is available in the online journal.)

5.2.2. Hot Gas Evolution with AGN-like Outbursts

In the recent past, NGC 4278 could have experienced a nuclear outburst with a high $\dot{m}$, and the high central value of the gas temperature could be a remnant of that episode. Indeed, the inner $\sim 4''$ seems to contain a hot bubble, a region that appears to be overpressured with respect to its surroundings. The absence of H I absorption against the nucleus (van Gorkom et al. 1989) suggests that the region around the center could have been cleared of neutral gas. Inspection of the *HST* WFPC2 images shows that the filamentary dust structure, which seems to spiral into the center (Section 5.3), is interrupted and becomes absent within a radius of $\sim 2''$; the color from the F330W and F450W images becomes bluer toward the center, where a point-like bright nucleus is seen (see also Lauer et al. 2005). Also, the ACS F439W and F850LP filter images show the nucleus sitting in a small unobscured hole at the center of a thin dust disk. All these are evidence for unusual conditions close to the nucleus, suggesting an interaction between the MBH and its surroundings, which could have occurred on a very local scale. For example, in an inner region the cooler gas could have been removed, thus there is no dust and no H I absorption around the nucleus (as also revealed by the X-ray spectral results; Section 4.1).

The effects of AGN feedback typical of accretion at high $\dot{m}$ have been investigated in detail previously with spherically symmetric hydrodynamical simulations (Ciotti et al. 2010). During outbursts, very hot central gas is created (within $\sim$100 pc), at a temperature that can reach up to a few keV; this central bubble is surrounded by gas at a much lower temperature (kT drops down to 0.3–0.4 keV at $\sim$1 kpc; Pellegrini et al. 2012), which resembles the observed trend in NGC 4278. However, there are two caveats. The first is that the hot bubble lasts for a short time ($<10^8$ yr), since it cools quickly and, soon after it is created, the accretion rate drops; furthermore, the outburst produces a low-density region surrounding the nucleus, with an almost flat 0.3–2 keV brightness profile, extending to a few kpc and lasting for $\sim 10^8$ yr (Pellegrini et al. 2012), and this large plateau in the brightness profile is not observed here (Figure 2(c)). The second caveat is that high $\dot{m}$ outbursts are coupled with star formation in the galactic central region, but NGC 4278 shows a uniformly old stellar population, without signs of current or recent star formation (Shapiro et al. 2010; Kuntschner et al. 2010). All these support the idea that nuclear outbursts at high $\dot{m}$ are well confined to the past. In fact, an isolated galaxy of the mass of NGC 4278 is expected to have a very small duty cycle for the phases of accretion at high $\dot{m}$, over the past few Gyr, with the last bursting episode confined to a few Gyr ago (Ciotti & Ostriker 2012).

As these simulations with accretion at high $\dot{m}$ show, after an outburst is terminated, a new sub-Eddington accretion phase is established, where the nucleus is radiatively quiescent ($\dot{m}$ is in the range of the RIAF regime). The galactic center, almost devoid of gas, is replenished with the newly injected stellar mass losses that feed the accreting flow and are kept hot by the MBH via compression, stellar heating, and the energy output from accretion. The gas behavior during this phase is similar to that described in Section 5.2.1, and the temperature profile resembles that obtained without feedback at an epoch of 10.9 Gyr in Figure 10 (Pellegrini et al. 2012); there is, however, less hot gas (at the same age). Therefore, even a post-outburst radiatively quiescent phase is not likely to explain the observed gas properties.

The models considered in this section include feedback expected from high $\dot{m}$ accretion that is in radiative and mechanical form, with the latter from AGN winds only. At low $\dot{m} \ll 0.01$ the bulk of the accretion output is thought to be mostly mechanical, emerging in the form of jet/outflows rather than radiation (e.g., Merloni & Heinz 2008). Given the presence of a parsec-scale jet in NGC 4278, we examine in Section 5.2.3 whether a central hot region can be produced by mechanical heating. Note that the different temperatures but very similar densities observed in the $2''$–$4''$ annulus in the two NW–SE and NE–SW directions (Figures 8 and 9) imply a variation in the thermal gas pressure from one quadrant to the next, at this fixed distance from the center: The pressure is higher perpendicular to the direction of the gas elongation (where the temperature is higher). The heating may have taken place along this preferential direction (the NW–SE one), which is also close to the jet directions (Figure 4).

5.2.3. Jet Heating (and Confinement)

VLBA observations of the NGC 4278 nucleus with a resolution of a few mas ($\sim$0.1 pc) at 5 and 8.4 GHz revealed synchrotron radio emission from a two-sided structure, made of two symmetric S-shaped jets emerging from a flat-spectrum core (Giroletti et al. 2005; see also Falcke et al. 2000). In total, the two-sided jet extends over $\sim$45 mas, which is 3.5 pc. The distance reached by the currently observed jets is then smaller than the accretion radius ($r_{\rm acc} \sim$ 15–25 pc; Section 5.1), and much smaller than the size of the observed hot region (which extends out to $4''$, in the NW–SE direction).

The mildly relativistic velocity for the jet ($v_j/c \approx 0.76$) implies an epoch of jet ejection that is 10–100 yr prior to the observation by Giroletti et al. (2005). These authors suggest that

this source does not evolve into a kiloparsec-scale radio galaxy, but rather ejects components that soon disrupt, without being able to travel long distances and form radio lobes. The lack of hot spots, which are instead prevalent in higher power compact symmetric objects, indicates that the relatively low-velocity jets may not be able to bore through the ISM and escape. The small size of the radio source was ascribed to a low-power central engine, which cannot create highly relativistic jets, possibly combined with the interaction with an ISM. We address then the following questions. What is the energy flux for the jets? Is it likely that they are frustrated by the hot ISM in the nuclear region? Is it possible that (a fraction of) the jet energy has been deposited in this region, creating the hot central gas?

The average thermal pressure of the X-ray gas for the central $2''$ radius sphere is 5.8×10^{-10} dyn cm^{-2} (Table 5), a value comparable to the pressure in the atmospheres of hot gas-rich giant ellipticals, where the hot ISM often confines radio sources (e.g., Allen et al. 2006; Cavagnolo et al. 2010). We can estimate the minimum pressure for the jets of NGC 4278 from synchrotron theory, assuming energy equipartition between particles and magnetic field (e.g., O'Dea & Owen 1987). The spectral index of $a = -0.54$ ($S \propto \nu^a$) gives a good description of the emission over the whole radio band (VLA measurements are available from 74 MHz to 22 GHz), with a possible flattening below 408 MHz (Giroletti et al. 2005). Calculating a 74 MHz–22 GHz radio luminosity for the jets of 6.2×10^{38} erg s^{-1}, and assuming a volume emitting region for the jet that is a cylinder of height 45 mas and radius $r_j = 4$ mas, with filling factor $\phi = 1$, gives $p_{\rm min} \sim 2 \times 10^{-6}$ dyn cm^{-2}. Then the jets can be thermally confined only if within a few parsecs the thermal pressure becomes much larger than average for the central $2''$ (=156 pc). However, this $p_{\rm min}$ value is likely uncertain (e.g., due to the unknown source volume). An alternative way to estimate the jet internal pressure p_j is via the energy flux carried by a jet, that is, via the jet power $P_{\rm jet} \approx 4\pi r_j^2 v_j \gamma_j^2 p_j$, with γ_j the jet Lorentz factor (e.g., Owen et al. 2000). $P_{\rm jet}$ can be estimated from its relationship with the 5 GHz radio core luminosity (Merloni & Heinz 2007); for an average $P_{5\ \rm GHz} = 4.5 \times 10^{37}$ erg s^{-1} for the core component resolved by the VLBA (Giroletti et al. 2005), the relation gives $P_{\rm jet} = 2.5 \times 10^{42}$ erg s^{-1}. Cavagnolo et al. (2010) also presented a relationship between the total synchrotron power at 200–400 MHz and the mechanical power of jets, measured from the cavity power. For a total $P_{200-400\,\rm MHz} = 4.7 \times 10^{37}$ erg s^{-1}, $P_{\rm jet} = 1.1 \times 10^{42}$ erg s^{-1}. The jet power, again inferred from the cavities observed in the hot ISM of nearby radio ellipticals, also correlates with the accretion power $L_{\rm acc} = 0.1 \dot{M}_B c^2$ (Allen et al. 2006). Inserting into this correlation the average $\dot{M}_B \sim 2.1 \times 10^{-3}\ M_\odot$ yr^{-1} of Section 5.1, one finds $P_{\rm jet} = 1.8 \times 10^{42}$ erg s^{-1}, in good agreement with the values given by the scalings with the radio luminosity. Note that these $P_{\rm jet}$ estimates imply a jet production efficiency $\epsilon_{\rm jet} = P_{\rm jet}/\dot{M}_B c^2 \approx 0.01$–$0.02$, that is, $P_{\rm jet}$ is a significant fraction of $L_{\rm acc}$. Unless $P_{\rm jet}$ is largely overestimated, mass needs then to be accreted at approximately the Bondi rate, derived for the gas properties close to the accretion radius; large reductions in the rate along the way to the MBH are not allowed (see also Allen et al. 2006). This completes the findings of Section 5.1 about the origin of the nuclear L_X, excluding the possibility that $\dot{M}_B$ is reduced by orders of magnitude.

Adopting $P_{\rm jet} \sim (1$–$2) \times 10^{42}$ erg s^{-1}, $\gamma_j = 1.5$, and $v_j = 0.76c$ (Giroletti et al. 2005), $p_j \sim (1.6$–$3.3) \times 10^{-6}$ dyn cm^{-2}. To overcome this pressure, within a few parsecs from the MBH, the product nT of the hot gas should increase by a factor of $\gtrsim 10^3$ above the average within $2''$. Whether this is indeed verified remains beyond testability with *Chandra*, but could be feasible within a factor of a few; for example, in a Bondi flow with $\gamma = 4/3$, the thermal pressure is $\propto r^{-2}$ and can then increase by a factor of $\sim 10^3$ moving inward by a factor of ~ 30 in radius; in an RIAF, the behavior of the pressure is similar (Narayan & Fabian 2011). Other cooler gas phases may contribute to the confinement of the jets as cold gas (e.g., Emonts et al. 2010); however, there is no evidence for their presence toward the nucleus, as discussed in Section 5.2.2. Alternatively, $P_{\rm jet}$ derived from the correlations above may be overestimated. If confinement is not feasible, the currently observed jets are really very young and just making their way through the hot ISM. Note, though, that extended radio emission out of the nucleus has not been detected, and that going down to the lowest frequency observed ($\sim$0.1 GHz), where "old" radio lobes should contribute if present, producing an excess of emission, the radio spectrum does not steepen, but rather, if anything, it flattens (e.g., Giroletti et al. 2005). From the relationship between a critical frequency above which the spectrum steepens due to ageing, in this case <1 GHz, and the electron age, one derives that old, extended emission must date back to at least a few $\times 10^8$ yr (for a magnetic field of a few μG, which is reasonable for an old radio lobe; e.g., Feretti & Giovannini 2008). Past radio activity seems then to have always been confined within the nuclear scale, or it took place more than a few $\times 10^8$ yr ago.

A jet could have heated the central gas via dissipation of the kinetic energy of shocks produced in the circumnuclear region. The heating by the jet of a region much larger than its currently observed extension requires that the activity phase started long before the estimated age (10–100 yr) for the component farthest from the nucleus. In fact, a plausible time to heat the gas is at least of the order of the sound crossing time t_s, and $t_s \sim 4 \times 10^5$ yr to cross the hot center out to $R = 2''$; $t_s \sim 10^6$ yr to reach $R = 4'' = 312$ pc. Heating of the center then requires at least $\sim 10^6$ yr. An upper limit to the time elapsed since the heating episode is given by the radiative gas cooling time for the center, $t_{\rm cool} = 3kT/2n\Lambda(T, Z)$, where $\Lambda(T, Z)$ is the cooling function (taken here from Sazonov et al. 2005). For the innermost $2''$, $t_{\rm cool} \sim 10^7$ yr and $t_{\rm cool}$ is a factor of ~ 3 longer for the surrounding annulus. Then, a radio outburst should have heated the gas not longer than $\sim 10^7$ yr ago. Indeed, in the hypothesis that this source is continuously ejecting components from the core that soon disrupt and cannot get out of the nucleus, heating may be frequent and confined to the galactic central region, keeping the gas hot there. The outburst duration in bright radio sources is quite well constrained to be 10^7–10^8 yr (e.g., Worrall 2009); the outburst recurrence time, for radio sources with $L_{1.4\ \rm GHz} > 10^{25}$ W Hz^{-1}, is such that each source is retriggered once every 0.5—few Gyr (Best et al. 2005; Worrall 2009). For lower luminosity sources, both the lifetimes and the recurrence times are more uncertain; it seems that the activity must be more frequently retriggered (Best et al. 2005). NGC 4278 could then be an extreme case of frequent triggering of low-power jet components.[20]

The final question is whether a past radio outburst could have injected enough heating to produce at least the thermal energy of the central hot region currently observed, $E_{\rm th} = 4.1 \times 10^{53}$ erg (within $2''$; Table 5). A jet power of the order of that estimated

[20] Note that a hot accretion flow (as considered in Sections 5.1 and 5.2.1) may well have resumed after a major heating episode $\lesssim 10^7$ yr ago, since the flow time from $r_{\rm acc} \sim 20$ pc to the center, at the free-fall velocity, is $\lesssim 10^5$ yr.

here, $P_{\rm jet} \sim (1\text{–}2) \times 10^{42}$ erg s^{-1}, can account for $E_{\rm th}$ in 0.4–1$\times 10^4$ yr, a time much lower than typical lifetimes of individual radio sources (see above); clearly, this requires that the whole $P_{\rm jet}$ is transferred to the ISM. $P_{\rm jet}$ is also far higher than the gas luminosity within 2″ (1.0×10^{39} erg s^{-1}) and within 4″ (1.16×10^{39} erg s^{-1}).

5.2.4. Hot Nuclei in Other Early-type Galaxies

In four other spheroids, *Chandra* observations revealed a clear temperature increase toward the center. All these cases reside in low-power radio galaxies ($L_{\rm radio} < 2 \times 10^{38}$ erg s^{-1}), or where the radio emission is not detected at all. The first one was Sombrero (NGC 4594; Pellegrini et al. 2003), where the LINER nucleus of L(2–10 keV) $= 1.5 \times 10^{40}$ erg s^{-1} is embedded in 0.7 keV gas, out to $r \sim 160$ pc, and then surrounded by $kT \lesssim$ 0.4 keV gas. This nucleus also hosts a compact radio source of low luminosity ($L_{15\ \rm GHz} = 1.58 \times 10^{38}$ erg s^{-1}). An increase in the central temperature was found in NGC 4649 (Humphrey et al. 2008), peaking at ∼1.1 keV within the innermost 200 pc, and dropping to ∼0.8 keV outside; NGC 4649 is a faint radio source extending for ∼4 kpc ($L_R = 1.4 \times 10^{37}$ erg s^{-1}; Dunn et al. 2010). The nuclear spectrum of the Virgo elliptical NGC 4552 includes a power law from the AGN plus a thermal plasma with $kT = 1.04$ keV; 5 GHz VLBA observations reveal a two-sided extended emission, suggestive of a parsec-scale jet-like structure, of total radio luminosity of 1.55×10^{38} erg s^{-1} (Machacek et al. 2006). Finally, a projected temperature of 0.65 keV within 2″ and 0.40 keV within 2″–4″ (for $d =$ 9.7 Mpc) was found in NGC 3115 (Wong et al. 2011), with $L_X < 10^{38}$ erg s^{-1} and no detected radio emission; the rise in the central temperature was attributed to the accretion flow.

A central temperature significantly higher than in the surroundings may then be a typical feature appearing during the activity cycle commonly followed by early-type galaxies in the local universe. It could be the sign that sometimes, in the life cycle of low-power objects, the jet cannot bore out of the nucleus' surroundings, but it can heat them.

5.3. The Extended, Misaligned Hot Gas, and the Colder Phases

One of the new and interesting findings from the deep observation of NGC 4278 is the presence of hot gas, with a spatial distribution more elongated than the optical one, and also misaligned with it (Figures 1 and 4). The soft diffuse X-ray emission instead seems to be aligned with that of the ionized gas, residing in a rotating disk or spiral, of semimajor axis length of ∼25″ (∼2 kpc; Figure 4; Sarzi et al. 2006; see also Osterbrock 1960; Goudfrooij et al. 1994). Thus, there is a spatial association (in projection) between the hot and the ionized gas phases: both show an elongated distribution, following the direction described by the same position angle, and misaligned with respect to the optical major axis. The SAURON data show that the ionized gas velocity field is regular, consistent with circular gas motions in a low inclination disk, with a deviation from this simple situation in the outer measured region, due to a gradual twisting of the velocity field. The gas is rotating in the same sense as the stars, but with a kinematic misalignment of a median angle of 29° ± 19° within 22″; the gaseous and stellar kinematics are misaligned by increasingly wider angles toward the outer parts of the field (Sarzi et al. 2006). The ionized gas is not rotating in the equatorial plane of the galaxy, and its distribution and kinematics are likely tracing gas that is accumulating while flowing in (Sarzi et al. 2006). Note that the SAURON angular resolution (each pixel is ∼1″ wide) was adequate to establish that the ionized gas is diffuse and not filamentary (see also Goudfrooij et al. 1994).

NGC 4278 also contains a large H I mass ($6.9 \times 10^8\ M_\odot$; Section 1), residing in a large regular disk or ring (Raimond et al. 1981), extending for 37 kpc, which implies that the system is old and evolved; the tails from the disk, revealed by a deep map, indicate that the system is still accreting gas (Morganti et al. 2006). Notwithstanding the extensive reservoir of neutral hydrogen and the very regular disk kinematics suggesting that the galaxy has been surrounded by cold gas for a few Gyr, there is no evidence for the presence of a young stellar population. Studies from various groups report a uniformly old age, from scales of $R_e/16$ to the whole galaxy (Terlevich & Forbes 2002; Kuntschner et al. 2010; Shapiro et al. 2010). Therefore, rather than recent merging with star formation, smooth accretion from outside is suggested, with the gas spread over a large area, diluted and resulting in the formation of little CO emission and hence no star formation (Morganti et al. 2006; CO emission is not detected, Crocker et al. 2011).

The H I disk extends down to the innermost resolution element of the Westerbork observation (≈2 × 1 kpc), where the ionized gas resides; in the more central regions, the H I and the ionized gas are suggested to be physically associated, since they are spatially and kinematically consistent (Morganti et al. 2006; Goudfrooij et al. 1994). Given this, and the fact that the radial profile of the Hβ flux can be fully explained by photoionization by the LINER nucleus only within the central 3″, but is clearly more extended than that, the ionized phase could be produced by shock heating of the accreting gas (Sarzi et al. 2010; see also Eracleous et al. 2010b). A weak triaxial perturbation of the stellar potential could funnel the gas into preferential streams, where fast shocks between gas clouds may occur. A problem with this origin for the warm gas is that shock velocities as high as required to power the observed line emission are not expected in the potential of NGC 4278; other diffuse sources of ionization, such as a hot ISM or old post-AGB stars, were then suggested to contribute or be dominant (Sarzi et al. 2010).

Finally, NGC 4278 shows a complex and irregular dust structure in its core, with several dense knots, interconnected by filaments, and prominent patchy dust out to ∼25″, mostly on the northern side of the nucleus; closer to the galactic center, due to a spiral pattern, the dust appears to be streaming toward the nucleus (Goudfrooij et al. 1994; Carollo et al. 1997; Lauer et al. 2005). *Spitzer* images revealed extended emission from warm dust, molecular hydrogen, and ionized gas (see Figure 4(b)), and IRS spectral observations shows excitation and ionization in the mid-IR (Tang et al. 2011). An inspection of the *HST* ACS F439W and F850LP filter images shows that the inner dust resides in a thin, moderately inclined disk, whose major axis aligns with the soft X-rays, optical emission line, and 8 μm emission.

Ionized gas, cold gas, and dust then seem to be different phases of the same accretion process of gas from outside; moreover, the diffuse X-ray emission follows the general pattern of the [O III] and 8 μm emission, and thus is likely to be associated with the other phases (Figure 4). Is the hot gas interacting with these phases, and does its elongation find an explanation in this interaction? In fact, the flattening of the diffuse X-ray emission with respect to the optical surface brightness, and even more its misalignment, are an unexpected result: the hot gas originates in the stars, and at equilibrium its density should follow the isopotential surfaces, which are

rounder than the optical isophotes, for reasonable galaxy models (e.g., Binney & Tremaine 1987). The origin of the hot gas elongation is not likely to reside in the presence of significant rotational support, inherited from the stars, from which the hot gas comes: in NGC 4278 only the inner galactic region is occupied by a fast stellar rotator, with a maximum rotation of ∼70 km s^{-1} at $0.4R_e$, and steeply decreasing outside. Also, the stellar kinematical axis is misaligned with respect to an axis perpendicular to the hot gas elongation (Figure 4). Another potential contributing factor for the hot gas elongation could be an AGN outflow, if it cleared the ISM along directions perpendicular to the observed hot (and warm) gas elongation, in a sort of bipolar outflow (e.g., Novak et al. 2011). Since the ionized gas disk has a modest inclination, such an AGN outflow, while not ruled out, seems less likely; also, no significant kinematic disturbance is seen in the [O III] SAURON velocity field, and then the elongated X-ray emitting region seems more a zone of enhanced emission. We also note that the same correlation between the X-ray emission, ionized gas, and 8 μm emission in a flattened structure (Figure 4) may be indicative of a dynamically supported ISM substructure (i.e., a gaseous bar, or warp, or some combination) located within the inner region of NGC 4278. Even in this model the X-ray feature is not directly associated with the directionality of the AGN jets.

The energy flux from the hot to the cold gas, by increasing the X-ray emissivity, could be the reason why the hot gas does not seem to be cospatial with the stellar distribution, but instead well aligned with the warm gas. The cold gas, accreting more or less steadily for a few Gyr, created within the galaxy a disk (or bar-like) region where the hot gas is made to cool preferentially, thus showing more emission there (e.g., Fabian et al. 2003). Thermal conduction is a specific example of an energy flux mechanism, and it has often been suggested to cause energy to flow from the hot coronal gas into colder gas in elliptical galaxies and galaxy clusters (Sparks et al. 1989; Macchetto et al. 1996; Fabian et al. 2003). Some of the ionized emission could result from the cold accreting material that is being excited by the hot gas during the evaporation process expected from the interaction between cold and hot gas. Thermal electron conduction excites the cold gas into optical emission, and locally enhances the X-ray emissivity and cools the hot gas; for example, two temperatures are present in the X-ray gas of M87, with the lower one in the vicinity of optical filaments (Sparks et al. 2004). Thus, electron conduction could also explain, at least in part, the discrepancy between the model and the observed temperatures out to a few hundreds pc. We examine next the energetics involved more quantitatively.

Under the assumption that the energy flux is in the saturated regime (Cowie & McKee 1977), the energy available to excite the optical emission is $Q_{\rm sat} = 5.2 \times 10^{40} T_7^{3/2} n_{0.01} D_{\rm maj} D_{\rm min}$, where $T_7 = T/10^7$ K is the hot gas temperature, $n_{0.01} = n_e/0.01$ cm^{-3} is its density, and $D_{\rm maj} D_{\rm min}$ is proportional to the apparent projected surface area ($D_{\rm maj}$ and $D_{\rm min}$ being the major and minor diameter of the line emitting region in kpc; Macchetto et al. 1996). The Hα emission line flux that is produced is $L \sim 10^{39} T_7^{3/2} n_{0.01} D_{\rm maj} D_{\rm min}$, if 1% of $Q_{\rm sat}$ is radiated in the Hα line, and the total surface area is twice the apparent projected surface area (this is a conservative assumption that applies to the observed ellipse shown in projection by the disk, whose depth along the line of sight and thickness remain unknown). The gas temperature and density outside the central 3″ radius, where the LINER has been shown to fully account for the ionization (Sarzi et al. 2010, their Figure 4), are $T_7 = 0.37$ (for $kT = 0.32$ keV) and $n_{0.01} = 1$; for $D_{\rm maj} \sim 4$ kpc and $D_{\rm min} \sim 2$ kpc (Figure 4), one has $L \sim 10^{39}$ erg s^{-1}. The total Hα luminosity observed is 9.1×10^{39} erg s^{-1} (rescaled for our adopted distance), and 5.8×10^{39} erg s^{-1} of this comes from outside the central 3″ radius (from data kindly provided by M. Sarzi). Thus, the energy flux does not violate the limit given by the observed line emission while contributing to the ionization of the extended warm gas distribution.

The presence of thermal conduction could also explain why the hot phase is colder than simple models predict, as shown by Figure 10 (Section 5.2.1). The total energy flux from the hot gas to the cold one, $Q_{\rm sat}$, turns out to be $\sim 10^{41}$ erg s^{-1}, a non-negligible amount. For example, SNIa heating for the whole galaxy amounts to 10^{41} erg s^{-1} at an age of 10 Gyr. Indeed, remarkably, the hot gas temperature seems close to just the stellar heating prediction (Figure 10), without traces of additional (e.g., from SNIa) heat sources.

The timescale for this process of heat transfer from hot to cold gas (or the evaporation lifetime) is difficult to compute because of the unknown internal density and distribution of the H I gas; however, given that the H I is much more massive than the hot gas and still accreting, the process is not a fast, recent, and transient phenomenon (recall also that the hot gas is continuously replenished by stellar mass losses).

6. CONCLUSIONS

We analyzed a deep (579 ks) *Chandra* ACIS pointing of the radio compact elliptical galaxy NGC 4278, which hosts a two-sided parsec-scale jet. We detected soft X-ray emission from hot gas out to a radius of ∼5 kpc, with a 0.5–8 keV luminosity of 2.4×10^{39} erg s^{-1}, elongated and misaligned with respect to the stellar body. At the nucleus, AGN-like emission with a spectral shape consistent with that of previous pointings since 2004 ($\Gamma = 2.31 \pm 0.20$ and small intrinsic absorption) decreased by a factor of ∼18 since the first *Chandra* observation, reaching down to $L_{0.5-8\,\rm keV} = 2.5 \times 10^{39}$ erg s^{-1}. Hot gas is also present at the nucleus, with a temperature ($kT = 0.75$ keV) significantly larger than in the surrounding region, where $kT \sim 0.3$ keV. We investigated the relationships between nuclear emission, fuel availability, and mechanical energy output from accretion, as well as the interaction between the hot and cold gas phases, and obtained the following main results.

The low luminosity of the AGN ($L_{0.5-8\,\rm keV}/L_{\rm Edd} = 5.9 \times 10^{-8}$ in 2010) can be explained by a low radiative efficiency accretion flow, with mass accreting at a rate close to that of the Bondi accretion solution ($\dot{m}_B = (0.7\text{–}7) \times 10^{-4}$). An average $\dot{M}_B = 2.1 \times 10^{-3}\ M_\odot$ yr^{-1} corresponds to $L_{0.5-8\,\rm keV} \lesssim 5 \times 10^{40}$ erg s^{-1}, which is larger than observed; however, the effect of rotation in the gas close to the accretion radius alone can easily reduce this to $L_{0.5-8\,\rm keV} \lesssim 5 \times 10^{39}$ erg s^{-1}. Estimates of the jet power from scalings with the radio luminosity at 5 GHz and 200–400 MHz, and with $\dot{M}_B$, all agree, giving $P_{\rm jet} = (1\text{–}2) \times 10^{42}$ erg s^{-1}. This power requires that the rate of accretion $\dot{M}$ onto the MBH is not largely reduced with respect to $\dot{M}_B$.

The hot gas flow, followed using hydrodynamical simulations including heating by SNeIa and only gravitational effects from the MBH, is an outflow on the galactic scale during the entire evolution, consistent with the low observed hot gas content. There is also a small accretion region at the center, through which mass flows on the MBH at a rate consistent with the estimate of $\dot{M}_B$ at the present epoch. The MBH heats the surrounding gas on a much smaller region than observed,

and the large and sharp temperature increase at the center is not reproduced; also, out of the central ∼0.5 kpc the model temperature is higher than observed, indicating that SNIa heating is less important than assumed, or that the gas is cooling due to the interaction with other gas phases. An MBH outburst in the recent past due to accretion at high $\dot{m}$ would be supported by the finding of a central overpressured region in the hot gas, and of a central "hole" in the cooler gas phases; however, it is not likely to be the origin of the high central temperature, since it should have also left a flatter brightness profile than observed in the central galactic region, and traces of star formation.

A jet could have heated the central gas during a past activity episode that took place a time $\lesssim t_{\rm cool} \sim 10^7$ yr ago. Extended radio emission is not detected, and the radio spectrum does not show signs of older lobes, thus it is likely that also in the past radio outbursts have not succeeded in getting out of the central galactic region. The central temperature then may have originated from a frequent triggering of low-power jet components that remain confined within the nucleus. A high temperature at the center may be a typical feature appearing during the activity cycle of low-power objects, when the jet cannot bore out of the nucleus surroundings but it can heat them. Unless $P_{\rm jet}$ has been overestimated, the thermal confinement of the parsec-scale jets requires the hot gas pressure to increase by a large factor ($\gtrsim 10^3$) above its average over the central 156 pc. Other colder gas phases seem to have been cleared from the nuclear region.

On the galactic scale, there is a spatial association (in projection) between the hot, the cold, and the ionized gas phases, all elongated in the same direction, and misaligned with respect to the optical major axis. The accreting cold gas triggering the cooling of the hot phase could produce both the unusual elongation and misalignment of the X-ray emission, and the lower temperature of the hot gas with respect to the predictions of hydrodynamical simulations. Part of the ionized emission could result from the cold gas excited by the hot gas during the evaporation process.

Investigations of the interplay between the hot gas and the nuclear activity are fundamental in the context of understanding the MBH–host-galaxy coevolution; NGC 4278 is the first case of a low-/medium-mass galaxy with a modest hot gas content that has been explored in detail using *Chandra* observations. Though expensive in terms of exposure time, other studies of similar objects are very much needed to build a coherent and comprehensive picture of accretion in the local universe. The interplay between the different gas phases, a result obtained from multiwavelength observations, is another field rich in consequences for our knowledge of the galactic ecology and evolution, and allowed here for a more exhaustive explanation of the hot gas properties as well.

We thank L. Ciotti, G. Giovannini, and R. Sancisi for useful discussions, and M. Sarzi for kindly providing data and the ionized gas images used for Figure 4. We thank the Aspen Center for Physics for hospitality and for providing a forum for discussion; this research has been partially supported by the National Science Foundation under grant No. 1066293. Partial financial support by the *Chandra* GO Grant GO0-11102X (PI: Fabbiano) and NASA Contract NAS8-39073 (CXC), and from the ASI-INAF Grant I/009/10/0 (G.T. and S.P.) is also acknowledged. The data analysis was supported by the CXC CIAO software and CALDB. We have used the NASA NED and ADS facilities and have extracted archival data from the *Chandra* archives.

Facility: *CXO* (ACIS)

APPENDIX

The hot gas flow in NGC 4278 has been investigated in Section 5.2.1 with spherically symmetric hydrodynamical simulations following the evolution of the stellar mass losses from a single burst passively evolving stellar population. This is a reasonable model thanks to the regular optical appearance of NGC 4278, a roundish galaxy with a uniformly old stellar population (see the Introduction). The galaxy model for the simulations, including a central black hole and stellar and dark mass components, was built as follows. The stellar density was derived from the surface brightness profile in the *I* band from *HST* WFPC2 *F814W* images and large-field ground-based photometry (Cappellari et al. 2006). This profile extends from 152″ down to $R \approx 0\farcs05$, within which the optical AGN dominates; within a radius of 1″ the profile flattens in a core; the effective radius is $R_e = 32''$ (equivalent to 2.496 kpc). For the distance adopted here, the *I*-band luminosity is $L_I = 3.4 \times 10^{10}\ L_{\odot,I}$ using the total observed magnitude $I_T = 8.83$, after correction for extinction (Cappellari et al. 2006). By spherical deprojection of this surface brightness profile we derived the 3D radial trend of the stellar density profile. The adopted central stellar velocity dispersion σ_0 was the observed luminosity-weighted velocity dispersion within a circular aperture of radius $R_e/8$, $\sigma(<R_e/8) = 252$ km s^{-1} (Kuntschner et al. 2010; Table 1). In the modeling of the total mass distribution, we imposed this σ_0 value on the projected and luminosity-weighted average of the stellar velocity dispersion within a circle of radius $R_e/8$.

The dark halo was chosen to have a Navarro et al. (1997) profile ($\rho_h \propto 1/(r/r_h)(1 + r/r_h)^2$, with r_h being the scale radius and truncated at large radii), and a total mass M_h. The free parameters M_*, r_h, M_h are determined by imposing the σ_0 value and the total mass-to-light ratio within R_e derived from models of NGC 4278, $M/L_I = 4.5$–5.2 (Cappellari et al. 2006), which implies a dark-to-luminous mass ratio within R_e, ($\mathcal{R}_e$), of 0.5–0.7. By solving the Jeans equations numerically for the three mass components in the isotropic orbits case (e.g., Binney & Tremaine 1987; the stellar velocity dispersion of NGC 4278 is nearly isotropic; Cappellari et al. 2007), with a central MBH acting as a point mass of $M_{\rm BH} = 3.4 \times 10^8\ M_\odot$ (Table 1), the resulting model has a stellar mass-to-light ratio of $M_*/L_I = 4.0$, $\mathcal{R}_e = 0.69$, and $\mathcal{R} = M_h/M_* = 3.5$ (in good agreement with $\mathcal{R} \approx 3$ at $10R_e$; Bertola et al. 1993; Kronawitter et al. 2000). Figure 11 shows the main dynamical properties of the adopted mass model.

The time evolving input ingredients of the simulations are the rate of stellar mass loss from the aging stellar population ($\dot{M}_*$) and the rate of SNIa heating ($L_{\rm SN}$). The mass return rate prescribed by the stellar evolution theory is used, as well as its decline as a function of time, computed following the prescriptions of Maraston (2005) for solar abundance and the Kroupa initial mass function (Pellegrini 2012). The present-epoch SNIa rate for nearby early-type galaxies is adopted, i.e., $0.16h_{70}^2$ SNu (where 1 SNu = 1 SNIa per 100 yr per $10^{10}\ L_{B,\odot}$, $h_{70} = H_\circ/70$; Cappellaro et al. 1999; Li et al. 2011a). The secular evolution of the rate is taken to be $\propto t^{-s}$, with $s = 1.1$, as suggested by recent large supernova surveys and modeling (e.g., Maoz et al. 2011). Another source of

heating for the stellar mass losses is the thermalization of stellar random motions, referred to as "stellar heating" in Section 5.2.1; this corresponds to a gas mass-weighted temperature of $T_\sigma = \frac{1}{k}\frac{\mu m_p}{M_*}\int 4\pi r^2 \rho_*(r)\sigma^2(r)\,dr$, where k is the Boltzmann constant, μm_p is the mean particle mass, $\sigma(r)$ is the 1D velocity dispersion of the stars, and $\rho_{\rm gas}(r) \propto \rho_*(r)$ is assumed, where $\rho_*(r)$ is the stellar density profile (see Pellegrini 2012 for more details).

The evolution of the galactic gas flow is obtained by integrating the time-dependent Eulerian equations of hydrodynamics with the above described source terms using a numerical code described in Pellegrini (2012), with a sink of the hydrodynamical quantities at the galactic center and no feedback effects from the central MBH. We adopt a central grid spacing of 5 pc for a good sampling of the inner regions, even within the Bondi radius, and a total of 240 logarithmically spaced grid points. The simulations begin at an age of 2 Gyr for the stellar population, when the galaxy has completed its formation process and the galactic wind phase driven by Type II supernovae explosions has already started, and end at the age of NGC 4278, 10.7 ± 2.14 (Terlevich & Forbes 2002). Figure 12 shows the radial profiles of the main hydrodynamical quantities (velocity, temperature, and density) at the two epochs considered for Figure 10.

REFERENCES

Allen, S. W., Dunn, R. J. H., Fabian, A. C., Taylor, G. B., & Reynolds, C. S. 2006, MNRAS, 372, 21
Anders, E., & Grevesse, N. 1989, Geochim. Cosmochim. Acta, 53, 197
Baldi, A., Raymond, J. C., Fabbiano, G., et al. 2006, ApJS, 162, 113
Bertola, F., Pizzella, A., Persic, M., & Salucci, P. 1993, ApJ, 416, L45
Best, P. N., Kauffmann, G., Heckman, T. M., et al. 2005, MNRAS, 362, 25
Binney, J., & Tremaine, S. 1987, Galactic Dynamics (Princeton, NJ: Princeton Univ. Press)
Blandford, R. D., & Begelman, M. C. 1999, MNRAS, 303, L1
Bondi, H. 1952, MNRAS, 112, 195
Boroson, B., Kim, D.-W., & Fabbiano, G. 2011, ApJ, 729, 12
Brassington, N. J., Fabbiano, G., Kim, D.-W., et al. 2009, ApJS, 181, 605
Buote, D. A., & Fabian, A. C. 1998, MNRAS, 296, 977
Cappellari, M., Bacon, R., Bureau, M., et al. 2006, MNRAS, 366, 1126
Cappellari, M., Emsellem, E., Bacon, R., et al. 2007, MNRAS, 379, 418
Cappellaro, E., Evans, R., & Turatto, M. 1999, A&A, 351, 459
Carollo, C. M., Danziger, I. J., Rich, R. M., & Chen, X. 1997, ApJ, 491, 545
Cattaneo, A., Faber, S. M., Binney, J., et al. 2009, Nature, 460, 213
Cavagnolo, K. W., McNamara, B. R., Nulsen, P. E. J., et al. 2010, ApJ, 720, 1066
Ciotti, L., & Ostriker, J. P. 2012, in Hot Interstellar Matter in Elliptical Galaxies, ed. D.-W. Kim & S. Pellegrini (Astrophysics and Space Science Library, Vol. 378; Heidelberg: Springer), 83
Ciotti, L., Ostriker, J. P., & Proga, D. 2010, ApJ, 717, 708
Cowie, L. L., & McKee, C. F. 1977, ApJ, 211, 135
Crocker, A. F., Bureau, M., Young, L. M., & Combes, F. 2011, MNRAS, 410, 1197
David, L. P., Jones, C., Forman, W., et al. 2009, ApJ, 705, 624
Davis, J. E. 2001, ApJ, 562, 575
Diehl, S., & Statler, T. S. 2008, ApJ, 680, 897
Di Matteo, T., Allen, S. A., Fabian, A. C., Wilson, A. S., & Young, A. J. 2003, ApJ, 582, 133
Di Matteo, T., Springel, V., & Hernquist, L. 2005, Nature, 433, 604
Doe, S., Nguyen, D., Stawarz, C., et al. 2007, in ASP Conf. Ser. 376, Astronomical Data Analysis Software and Systems XVI, ed. R. A. Shaw, F. Hill, & D. J. Bell (Tucson, AZ: ASP), 543
Dunn, R. J. H., Allen, S. W., Taylor, G. B., et al. 2010, MNRAS, 404, 180
Elvis, M., Wilkes, B. J., McDowell, J., et al. 1994, ApJS, 95, 1
Emonts, B. H. C., Morganti, R., Struve, C., et al. 2010, MNRAS, 406, 987
Eracleous, M., Hwang, J. A., & Flohic, H. M. L. G. 2010a, ApJS, 187, 135
Eracleous, M., Hwang, J. A., & Flohic, H. M. L. G. 2010b, ApJ, 711, 796
Fabbiano, G., Baldi, A., Pellegrini, S., et al. 2004, ApJ, 616, 730
Fabbiano, G., Brassington, N. J., Lentati, L., et al. 2010, ApJ, 725, 1824
Fabian, A. C., Sanders, J. S., Crawford, C. S., et al. 2003, MNRAS, 344, L48
Falcke, H., Nagar, N. M., Wilson, A. S., & Ulvestad, J. S. 2000, ApJ, 542, 197
Feretti, L., & Giovannini, G. 2008, in A Pan-Chromatic View of Clusters of Galaxies and the Large-scale Structure, ed. M. Plionis, O. López-Cruz, & D. Hughes (Lecture Notes in Physics, Vol. 740; Dordrecht, The Netherlands: Springer), 143
Forman, W., Jones, C., Churazov, E., et al. 2007, ApJ, 665, 1057
Frank, J., King, A., & Raine, D. J. 2002, Accretion Power in Astrophysics (Cambridge: Cambridge Univ. Press)
Freeman, P. E., Kashyap, V., Rosner, R., & Lamb, D. Q. 2002, ApJS, 138, 185
Gallo, E., Treu, T., Marshall, P. J., et al. 2010, ApJ, 714, 25
Garcia, A. M. 1993, A&AS, 100, 47
Garmire, G. P., Bautz, M. W., Ford, P. G., Nousek, J. A., & Ricker, G. R., Jr. 2003, Proc. SPIE, 4851, 28
Giroletti, M., Taylor, G. B., & Giovannini, G. 2005, ApJ, 622, 178
Goudfrooij, P., Hansen, L., Jorgensen, H. E., & Norgaard-Nielsen, H. U. 1994, A&AS, 105, 341
Haardt, F., & Maraschi, L. 1993, ApJ, 413, 507
Ho, L. C. 2008, ARA&A, 46, 475
Ho, L. C. 2009, ApJ, 699, 626
Ho, L. C., Filippenko, A. V., & Sargent, W. L. W. 1997, ApJ, 487, 568
Hopkins, P. F., Hernquist, L., Cox, T. J., et al. 2005, ApJ, 625, L71
Humphrey, P. J., & Buote, D. A. 2006, ApJ, 639, 136
Humphrey, P. J., Buote, D. A., Brighenti, F., Gebhardt, K., & Mathews, W. G. 2008, ApJ, 683, 161
Igumenshchev, I. V., Narayan, R., & Abramowicz, M. A. 2003, ApJ, 592, 1042
Jarrett, T. H., Chester, T., Cutri, R., Schneider, S. E., & Huchra, J. P. 2003, AJ, 125, 525
Kaviraj, S., Schawinski, K., Silk, J., & Shabala, S. S. 2011, MNRAS, 415, 3798
Kim, D.-W. 2012, in Hot Interstellar Matter in Elliptical Galaxies, ed. D.-W. Kim & S. Pellegrini (Astrophysics and Space Science Library, Vol. 378; Heidelberg: Springer), 121
Kim, D.-W., & Fabbiano, G. 2003, ApJ, 586, 826
Kim, D.-W., Fabbiano, G., Brassington, N. J., et al. 2009, ApJ, 703, 829
Kim, D.-W., Fabbiano, G., Kalogera, V., et al. 2006, ApJ, 652, 1090
Kim, D.-W., Fabbiano, G., Matsumoto, H., Koyama, K., & Trinchieri, G. 1996, ApJ, 468, 175
Kronawitter, A., Saglia, R. P., Gerhard, O., & Bender, R. 2000, A&AS, 144, 53
Kuntschner, H., Emsellem, E., Bacon, R., et al. 2010, MNRAS, 408, 97
Lauer, T. R., Faber, S. M., Gebhardt, K., et al. 2005, AJ, 129, 2138
Li, W., Chornock, R., Leaman, J., et al. 2011a, MNRAS, 412, 1473
Li, Z., Jones, C., Forman, W. R., et al. 2011b, ApJ, 730, 84
Loewenstein, M., Mushotzky, R. F., Angelini, L., Arnaud, K. A., & Quataert, E. 2001, ApJ, 555, L21
Macchetto, F., Pastoriza, M., Caon, N., et al. 1996, A&AS, 120, 463
Machacek, M., Nulsen, P. E. J., Jones, C., & Forman, W. R. 2006, ApJ, 648, 947
Mahadevan, R. 1997, ApJ, 477, 585
Maoz, D. 2007, MNRAS, 377, 1696
Maoz, D., Mannucci, F., Li, W., et al. 2011, MNRAS, 412, 1508
Maraston, C. 2005, MNRAS, 362, 799
Mathews, W. G. 1990, ApJ, 354, 468
Merloni, A., & Heinz, S. 2007, MNRAS, 381, 589
Merloni, A., & Heinz, S. 2008, MNRAS, 388, 1011
Million, E. T., Werner, N., Simionescu, A., et al. 2010, MNRAS, 407, 2046
Morganti, R., de Zeeuw, P. T., Oosterloo, T. A., et al. 2006, MNRAS, 371, 157
Morrison, R., & McCammon, D. 1983, ApJ, 270, 119
Nagar, N. M., Wilson, A. S., & Falcke, H. 2001, ApJ, 559, L87
Narayan, R., & Fabian, A. C. 2011, MNRAS, 415, 3721
Narayan, R., & Yi, I. 1995, ApJ, 452, 710
Navarro, J. F., Frenk, C. S., & White, S. D. M. 1997, ApJ, 490, 493
Nemmen, R., Storchi-Bergmann, T., & Eracleous, M. 2011, ApJ, submitted (arXiv:1112.4640)
Novak, G. S., Ostriker, J. P., & Ciotti, L. 2011, ApJ, 737, 26
O'Dea, C. P., & Owen, F. N. 1987, ApJ, 316, 95
Osterbrock, D. E. 1960, ApJ, 132, 325
Owen, F. N., Eilek, J. A., & Kassim, N. E. 2000, ApJ, 543, 611
Pellegrini, S. 2005, ApJ, 624, 155
Pellegrini, S. 2010, ApJ, 717, 640
Pellegrini, S. 2011, ApJ, 738, 57
Pellegrini, S. 2012, in Hot Interstellar Matter in Elliptical Galaxies, ed. D.-W. Kim & S. Pellegrini (Astrophysics and Space Science Library, Vol. 378; Heidelberg: Springer), 21
Pellegrini, S., Baldi, A., Fabbiano, G., & Kim, D.-W. 2003, ApJ, 597, 175
Pellegrini, S., Baldi, A., Kim, D. W., et al. 2007a, ApJ, 667, 731
Pellegrini, S., Ciotti, L., & Ostriker, J. P. 2012, ApJ, 744, 21
Pellegrini, S., Siemiginowska, A., Fabbiano, G., et al. 2007b, ApJ, 667, 749

Proga, D., & Begelman, M. C. 2003, ApJ, 592, 767
Ptak, A., Terashima, Y., Ho, L. C., & Quataert, E. 2004, ApJ, 606, 173
Quataert, E. 2003, Astron. Nachr., 324, 435
Raimond, E., Faber, S. M., Gallagher, J. S., III., & Knapp, G. R. 1981, ApJ, 246, 708
Sarzi, M., Falcón-Barroso, J., Davies, R., et al. 2006, MNRAS, 366, 1151
Sarzi, M., Shields, J. C., Schawinski, K., et al. 2010, MNRAS, 402, 2187
Sazonov, S. Yu., Ostriker, J. P., Ciotti, L., & Sunyaev, R. A. 2005, MNRAS, 358, 168
Schawinski, K., Lintott, C. J., Thomas, D., et al. 2009, ApJ, 690, 1672
Schilizzi, R. T., Fanti, C., Fanti, R., & Parma, P. 1983, A&A, 126, 412
Shapiro, K. L., Falcón-Barroso, J., van de Ven, G., et al. 2010, MNRAS, 402, 2140
Silk, J., & Rees, M. J. 1998, A&A, 331, L1
Smith, R. K., Brickhouse, N. S., Liedahl, D. A., & Raymond, J. C. 2001, ApJ, 556, L91
Sparks, W. B., Donahue, M., Jordan, A., Ferrarese, L., & Côté, P. 2004, ApJ, 607, 294
Sparks, W. B., Macchetto, F., & Golombek, D. 1989, ApJ, 345, 153
Stone, J. M., Pringle, J. E., & Begelman, M. C. 1999, MNRAS, 310, 1002
Tang, S., Wang, Q. D., Mac Low, M., & Joung, M. R. 2009, MNRAS, 398, 1468
Tang, Y., Gu, Q., Zhang, S., & Tang, B. 2011, MNRAS, 414, 1827
Terashima, Y., & Wilson, A. S. 2003, ApJ, 583, 145
Terlevich, A. I., & Forbes, D. A. 2002, MNRAS, 330, 547
Tonry, J. L., Dressler, A., Blakeslee, J. P., et al. 2001, ApJ, 546, 681
Tremaine, S., Gebhardt, K., Bender, R., et al. 2002, ApJ, 574, 740
van Gorkom, J. H., Knapp, G. R., Ekers, R. D., et al. 1989, AJ, 97, 708
Wong, K.-W., Irwin, J., Yukita, M., et al. 2011, ApJ, 736, L23
Worrall, D. M. 2009, A&AR, 17, 1
Wrobel, J. M., & Heeschen, D. S. 1984, ApJ, 287, 41
Younes, G., Porquet, D., Sabra, B., et al. 2010, A&A, 517, 33
Yuan, F., & Cui, W. 2005, ApJ, 629, 408